GAMMA SPECTROSCOPY OF THE DOUBLY – ODD ^{194}Tl NUCLEUS

Tshifhiwa Marius Ramashidzha

Thesis presented in fulfillment of the requirements for the degree of Master of

Sciences in the Department of Physics at the

University of the Western Cape

Supervisor: Dr. E. A. Gueorguieva

Nuclear Physics Group

iThemba LABS

Co-supervisor: Prof. R. Lindsay

Department of Physics

University of the Western Cape

January 2006

DECLARATION

I, the undersigned, hereby declare that the work contained in this thesis is my own

original work and that I have not previously in its entirety or in part submitted it at

any university for a degree.

Signature: …………………………………………………

Date: …………………………………………………………

ABSTRACT

GAMMA SPECTROSCOPY OF THE DOUBLE – ODD ^{194}Tl NUCLEUS

Tshifhiwa Marius Ramashidzha

January 2006

iThemba LABS, P.O. Box 722, Somerset West, 7129, South Africa

The odd – odd Tl nuclei with A ≥ 190 have moderate oblate nuclear deformation and show rotational bands built on different quasiparticle excitations. Several phenomena, not yet fully understood, were observed in these nuclei, such as large signature splitting in the yrast band (built on a $\pi h_{9/2} \otimes \nu i_{13/2}$ configuration), possible non – axiality of the nuclear shape, etc. In this work the high – spin states in ^{194}Tl were studied. The ^{194}Tl nuclei were produced in the ^{181}Ta (^{18}O, 5n) ^{194}Tl reaction at a beam energy of 93 MeV and the γ - rays were detected using the AFRODITE array. The obtained extended level scheme of ^{194}Tl is presented and discussed in this work. CSM (Cranking shell model) and TRS (Total Routhians Surface) models were both applied to interpret the results for band 1. The results were compared with the neighboring isotone ^{193}Hg.

ACKNOWLEDGEMENTS

I wish to express my sincere gratitude to the following for making the realization of this thesis possible. I would like to specially thank my supervisors:

- Dr Elena Gueorguieva – Lawrie, a good supervisor who guided me through this work, supporting and encouraging me to work harder;
- Prof. R. Lindsay, supervisor, his important part in making this thesis a success through his support throughout the duration of the project;
- Dr J.J. Lawrie, for allowing me to pursue this project in the Physics Group and helping with the setting up of the AFRODITE electronics;
- Dr. R. A. Bark and Dr. S. M. Mullins, for their willingness to help with almost everything, ultimately getting the experiment to work;
- Mr. T. J. Sikhwari, Mrs. T.E. Sikhwari and Mr. A.R. Serongwa, for their invaluable help during my studies (especially financial) and with so many things. I owe them so much that it is difficult to express my sincere gratitude;
- My parents (Mr. J.M. Ramashidzha and Mrs. T.E. Ramashidzha), for their guidance, support and so many things, just being there for me in time I needed them most and for inspiring me in my studies;
- Mr. S. H. M. Murray, for his invaluable help during the data sorting using MIDAS;
- Mr. O. T. Shirinda, for helping me with the theoretical calculations;
- Ms. M.P. Mamafha, for inspiring me and giving me a strong courage especially when I am hopeless; showing me that life is a precious gift from God and with God everything is possible;
- Mr. S. M. Maliage, Mr. T. Malwela, Mr. F. S. Komati, Mr. K.P. Mutshena, Mr. .N.E. Maluta, Ms. L.J. Mudau, Mr. V.C. Maboyi, Mr. P. Vymers, and Mr. N. Botha, for their guidance and support throughout the duration of the project;
- Dr. I.P. Matamba, I would like to thank you very much for your efforts coming down from Venda to participate in my experiment;
- To all staff and postgraduates within the Physics Group;

UNIVERSITY *of the*
WESTERN CAPE

CONTENTS

LIST OF FIGURES

LIST OF TABLES

UNIVERSITY *of the*

WESTERN CAPE

CHAPTER 1

INTRODUCTION

This work presents a spectroscopic investigation of the high – spin states of the ^{194}Tl isotope. The odd – odd Tl nuclei with mass A > 190 have moderate oblate nuclear deformation and show rotational bands, built on different quasiparticle excitations [Kre77, Kre78, Kre79, Kre80, Kre80, Kre81]. The yrast bands in these nuclei are associated with the $\pi h_{9/2} \otimes v i_{13/2}$ configuration and include low – energy transitions near their bandheads. Since it is very difficult to detect such transitions with standard gamma – ray spectroscopy some uncertainty about the low – lying levels exists. (A description of the high – spin phenomena in ^{194}Tl is presented from both the experimental and theoretical points of view). The characteristic features of collective nuclear rotation motion, such as rotational bands, signature splitting, band crossing and backbending were studied. Many rare earth nuclei have been extensively investigated up to high spin by means of the (HI, xn) reactions. However, only states lying on or close to the yrast line can be observed in such reaction and no information about non – yrast low spin states can be obtained. The ^{194}Tl nuclei were populated via the complete fusion reaction ^{181}Ta (^{18}O, 5n) ^{194}Tl at beam energy of 93 MeV and the γ - rays were detected using the AFRODITE array. The purpose of this work was to extend the existing level scheme of ^{194}Tl to higher spins and to test the predictions of the TRS and CSM models for the yrast $\pi h_{9/2} \otimes v i_{13/2}$ band. The level scheme was established up to spin of 27 $\hbar$ and several new bands were found. About ~ 90 new transitions were placed in the level scheme. The experimental methods and results shall be presented in chapters 4 and 5 respectively. The cranked shell model (CSM) was successfully applied to the ^{194}Tl isotope with the aid of the TRS model. Calculated routhians, band crossing frequencies and aligned angular momenta were found in good agreement with the experimental values. However these models were unable to satisfactorily reproduce the observed signature inversion. The rest of the thesis is arranged as follows:

❖ Chapter 2 contains two theoretical models describing the rotational behaviour of the nucleus which are the TRS and CSM models.

❖ Chapter 3 explains the experimental equipment and techniques as well as the electronic set up. This chapter also mentions several types of nuclear reactions.

❖ Chapter 4 includes details on how the experiment was performed and on the data analysis.

❖ Chapter 5 contains the experimental results obtained on the level scheme of the ^{194}Tl nucleus and shows the extended level scheme of ^{194}Tl.

❖ Chapter 6 shows the experimental quantities calculated in a rotating coordinate system which were deduced from our level scheme of ^{194}Tl. The theoretical calculations performed with the TRS and CSM models are also presented in this chapter. A comparison of both experimental and theoretical results as well as a comparison with the neighboring ^{193}Hg isotone is also presented.

UNIVERSITY of the
WESTERN CAPE
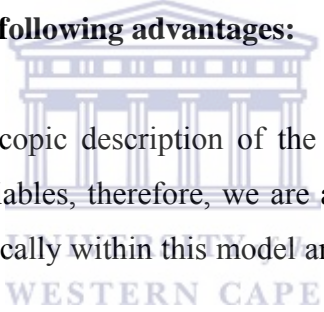
CHAPTER 2

THEORETICAL MODELS

2.1   Cranking shell models

The cranking shell model gives a fully microscopic description of the influence of the rotation on the single – particle motion of the nucleus. It provides a good description of the independent – particle motion in a rotating nucleus with both static deformed shape and pair fields [Nil95]. In such a rotating system fictive centrifugal and Coriolis forces emerge, resulting in important consequences for the shape and pair correlations [Ben85].

The cranking model has the following advantages:

(i) It provides a fully microscopic description of the rotating nucleus. There is no introduction of redundant variables, therefore, we are able to calculate the rotational inertial parameters microscopically within this model and get a deeper insight into the dynamics of rotational motion.

(ii) The collective angular momentum is described as a sum of single – particle angular momenta. Therefore, collective rotation as well as single – particle rotation, and all transitions in between such as decoupling processes, are handled on the same footing.

(iii) The model is correct also for very large angular momenta, where classical arguments apply [Ben83, Rin80].

The shortcomings of the model are:

(i) It is basically a nonlinear theory. Only in the limit of small angular momenta can one linearize it using perturbation theory (cranking formula for the moment of inertia). In general the calculations are therefore complicated, especially in cases where one has several solutions.

(ii) The resulting wave functions are not eigenstates of the angular momentum operators. It is therefore not clear a priory how one has to calculate, for example, electromagnetic transition probabilities. In fact, the cranking model wave functions are in a sense only internal wave functions and one has to use projection techniques to get the wave functions in the laboratory system.

The cranking model is one of the most useful, among theoretical models aiming at the description of high spin states in nuclei. It was originally proposed by Inglis [Ing54, Ing55], and was further developed by Bengtsson and Frauendorf [Ben79]. It combines in the same formalism the description of collective rotational bands and high – spin single – particle configurations, which are the two kinds of structures that are most important in the vicinity of the yrast line at high spins. In the following sections we shall discuss some aspects of the cranking model and show how it can be applied in some particular situations.

2.1.1   The cranking Hamiltonian

In the cranking model, the rotation is treated in the classical sense with the rotation vector coinciding with one of the main axes of the nucleus. The nucleus can be described as independent particles moving in a rotating potential. The calculations are then performed in the intrinsic coordinates of the rotating potential. A very direct way of investigating the properties of a rotating nucleus is to force it to rotate with some fixed frequency, ω, or in other word to "crank" the nucleus. The theoretical model emerging from this concept is therefore called the cranking model. The original derivation of the single – particle cranking Hamiltonian is based on a transformation of the time – dependent Schrödinger equation from the space fixed coordinate axes to the axes fixed with the rotating body. It is shown [Ing54, Ing55] and in many textbooks, for instance [Szy83, Voi83] that the Schrödinger equation in the rotating system can be solved in the standard way as an eigenvalue problem:

$$h_i^{\omega} = \left(h_i - \hbar\omega j_{i1}\right)\Psi_i^{\omega} = e_i^{\omega}\Psi_i^{\omega} \tag{2.1}$$

where

h is the single particle hamiltonian in the body – fixed non – rotating basis,

ω is the rotational frequency of the nucleus,

4

j_1 is the expectation value of the projection of the nucleon angular momentum along the rotation axis,

e^ω is the eigenvalue of the cranking hamiltonian for fixed rotational frequency ω. The eigenvalues are referred as single – particle energies in the rotating basis, or more properly as single – particle routhians. They can be found by taking the expectation value of the single – particle Hamiltonian h_i^ω as follows.

$$e_i^\omega = e_i - \hbar\omega j_{i1} \tag{2.2}$$

The total cranking Hamiltonian H^ω of the nucleus can be obtained by summing the single – particle cranking Hamiltonians h_i^ω. Thus

$$H^\omega = \sum_{i_{occ}} h_i^\omega = H - \hbar\omega I_1 \tag{2.3}$$

where I_1 is the aligned angular momentum i.e. the sum of the expectation values of individual angular momenta projected onto the rotational axis:

$$I_1 = \sum_{i_{occ}} j_{i1} \tag{2.4}$$

The eigenvalues E^ω of the total cranking Hamiltonian H^ω can correspondingly be written in terms of the independent single – particle contributions:

$$E^\omega = \sum_{i_{occ}} e_i^\omega \tag{2.5}$$

The total energy of the nucleus E^ω in the body – fixed frame system E^ω can consequently be called the routhian of the system and can be written as.

$$E^\omega = E - \hbar\omega I_1 \tag{2.6}$$

The lowest eigenstate E^ω corresponds to an yrast state and the sequence of these states obtained by enlarging ω constitutes the yrast line.

It should be noted that the operators H and I_1 do not have simultaneous eigenfunctions, implying mixing of the single – particle wave functions for ω ≠ 0. Further, the total spin I is not a good quantum number in these calculations. However an important advantage of CSM is that it provides a microscopic treatment of both

single – particle and collective phenomena and hence is very useful in the interpretation of experimental data [Ing55, Ben 79].

2.1.2   Symmetries of the cranking Hamiltonian

The theoretical treatment becomes simplest if we determine the quantum numbers necessary to describe a rotational state in a nucleus. It is important to discover the constants of the motion in the rotating system. This is done by noting which of the system observables commute with the cranking Hamiltonian H^{ω}. The symmetries of the Hamiltonian H^{ω}, describing the non – rotating nuclear system are apparent: there is invariance with respect to space and time inversion. By implication therefore, the parity π and the projection of nuclear spin Ω onto the symmetry axis are good quantum numbers in the absence of rotation. The space inversion yields the parity quantum number, whereas the time inversion gives rise to a two – fold degeneracy in nuclear systems, Kramer's degeneracy. Other symmetries can occur in nuclei, depending on the symmetries of the nuclear potential. Depending on the nuclear shape an invariance of the nuclear potential with respect to the rotations of 180° about the three principal axes of the system can occur. The rotation operators are given by:

$$R_k = e^{-i\pi j_k} \tag{2.7}$$

where k denotes the 1, 2 and 3, and j_k the projection of the single particle angular momentum j on the k axis.

Studying the symmetries of the cranking Hamiltonian H^{ω}, one can observe that:

(a) When the system is constrained to rotate, the time reversal symmetry is broken. This implies that the Kramer's degeneracy is broken and therefore another additional quantum number is needed to describe the system;

(b) Due to the rotation of the coordinate basis the invariance of the nuclear potential with respect to the rotation operators R_k is not valid in all cases. In particular, it is broken for R_2 and R_3 operators, since they do not commute with the operator j_1 of equation (1.1). On the other hand, the R_1 invariance still holds true and therefore one can introduce an additional quantum number, r, called signature, as the eigenvalue of this operator. Often another quantum number, α, is used, which is related to r by:

$$r = e^{-i\pi\alpha} \tag{2.8}$$

The R_1^2 is equivalent to a rotation of the system through the angle 2π. For odd – mass system, with anti – symmetric total wave function, ($R_1^2\psi = -\psi$), such a rotation implies that $r = \pm\ i$, corresponding to $\alpha = \mp\dfrac{1}{2}$. For an even – mass system the wavefunction is symmetric and similarly $r = \pm 1$, corresponding to $\alpha = 0$ and $\alpha = 1$ respectively. In practice the α quantum number is commonly used, since it is an additive quantity. A simple relation can be found between the total nuclear spin I and α [Boh75, Szy83].

$$I = 0,2,4,6,..., \quad r = 1, \quad \alpha = 0 \tag{2.9}$$

$$I = 1,3,5,7,..., \quad r = -1, \quad \alpha = 1 \tag{2.10}$$

$$I = \frac{1}{2},\frac{5}{2},\frac{9}{2}..., \quad r = -i,\ \alpha = 1/2 \tag{2.21}$$

$$I = \frac{3}{2},\frac{7}{2},\frac{11}{2}..., \quad r = +i,\ \alpha = -\ 1/2 \tag{2.22}$$

In summary:

$$I = \alpha,\ \alpha+2,\ \alpha+4,\ ... \tag{2.22}$$

The only remaining good quantum numbers after introduction of the cranking Hamiltonian are parity and signature (π, α). The classification of rotational spectra in terms of signature as a quantum number is essential in the high spin region. A band, classified for instance by the projection K of the intrinsic spin on the symmetry axis at low spin, separates in two bands at higher spins, each one labeled with a different value of signature α.

2.1.3   Comparison of the cranking model results and experimental data

In Cranked Shell Model (CSM) all parameters of the nuclear system like energy, angular momentum, etc. are calculated with respect to the rotating coordinate system, fixed with the principle axes of the nucleus, while experimentally measured values are obtained with respect to the laboratory system. In order to transform the experimental

data to the rotating frame, the total experimental Routhian must be defined. An expression for the total experimental Routhian is:

$$E^{\omega}_{\exp t}(I) = \frac{1}{2}\left[E(I+1)+E(I-1)\right]-\omega(I)I_x(I)$$

(2.23)

where I_x is the aligned angular momentum, given by the square – root term in the denominator of

$$\hbar\omega = \frac{dE(I)}{d\sqrt{I(I+1)-K^2}}$$

(2.24)

where $\sqrt{I(I+1)-K^2}$ is the projection of the total angular momentum onto the rotational axis, known as angular momentum, I_x. For $K=0$ rotational band of stretched $E2$ transitions this can be approximated by:

$$\hbar\omega = \frac{E_I - E_{I-2}}{\sqrt{I(I+1)}-\sqrt{(I-2)(I-1)}} \approx \frac{E_\gamma}{2} \text{ when } I \gg K.$$

(2.25)

Comparison between the total experimental Routhian and the theoretical quasi-particle Routhian requires the subtraction of an energy reference. A subtraction of this kind removes the contributions from the core, and leaves the experimental behavior of the quasi-particles. The experimental quasi-particle Routhian and alignment are defined by :

$$e^{\omega}_{\exp t}(I) = E^{\omega}_{\exp t}(I) - E^{\omega}_{ref}(I)$$

(2.26)

and

$$i^{\exp t}_x(\omega) = I_x\omega - I^{ref}_x(\omega).$$

(2.27)

The energy reference of the core can be calculated using a variable moment of inertia fit to the low-lying transitions as a function of ω^2 ;

$$I^{(1)}_{ref}(\omega) = J_0 + \omega^2 J_1$$

(2.28)

Where J_0 and J_1 are known as the Harris parameters [Har65]. The aligned angular momentum reference is given by

$$I_x^{ref}(\omega) = \frac{1}{\hbar}\left(J_0 + \omega^2 J_1\right)\frac{\omega}{\kappa} \qquad (2.29)$$

and the reference energy by:

$$E_x^{ref}(\omega) = -\frac{1}{2}\omega^2 J_0 - \frac{1}{4}\omega^4 J_1 + \frac{1}{8}\frac{\hbar^2}{J_0} \qquad (2.30)$$

The integration constant $\frac{\hbar^2}{8J_0}$ is introduced to ensure that the ground state reference energy is set to zero. The experimental alignment $i_x(\omega)$ and Routhian $e_{\exp t}^{\omega}(\omega)$ can be compared directly with the theoretical alignment and Routhian.

2.2   The Total Routhian Surface (TRS) calculations

The TRS calculations performed by R. Wyss [Wys90] were employed in this work. They were performed for the nuclei with $30 \leq Z \leq 84$, and for all possible combinations of the 16 lowest nucleons routhians. The data are stored as five different data bases for nuclei in the different regions, see table 1.2.

Table 2.1: The databases of the TRS calculations.

IMESH = 0	$30 \leq Z \leq 44$	$32 \leq N \leq 48$
IMESH = 1	$50 \leq Z \leq 62$	$60 \leq N \leq 78$
IMESH = 2	$58 \leq Z \leq 70$	$72 \leq N \leq 90$
IMESH = 11	$64 \leq Z \leq 74$	$84 \leq N \leq 104$
IMESH = 8	$72 \leq Z \leq 84$	$92 \leq N \leq 118$

2.2.1   The Model

The total routhian E_{tot}^{ω} (Z, N, $\hat{\beta}$) of a nucleus (Z, N) at a frequency ω and a deformation $\hat{\beta}$ is obtained within the cranked Wood – Saxon Bogolyubov – Strutinsky approach, as the sum of the macroscopic liquid – drop energy, the shell correction energy and the pairing correction energy:

$$E^{\omega}(Z, N, \hat{\beta}) = E_{LD}^{\omega}(Z, N, \hat{\beta}) + E_{shell}^{\omega}(Z, N, \hat{\beta}) + E_{pair}^{\omega}(Z, N, \hat{\beta}) \qquad (2.31)$$

For the liquid – drop macroscopic term the standard liquid – drop mass formula is used [Mye67]. The moment of inertia has the value of a rigid rotor with R = $1.23A^{1/3}$ fm.

The nuclear mean field is parameterized by a Wood – Saxon single – particle potential [Naz85] with the parameters of ref. [Dud81]. It contains a central potential, a spin – orbit term, and the Coulomb potential. The nuclear shape is parameterized in terms of quadrupole, hexadecapole and triaxial degrees of freedom, $\hat{\beta}$ ($\hat{\beta}$ is represent deformation). These, together with the BCS field parameters Δ_p and Δ_n for protons and neutrons, respectively, are treated as variational parameters.

Cranking implies that the system is constrained to rotate around a fixed axis with a given frequency ω. The routhian $\hat{H}^{\omega}$ is thus minimized at fixed deformation and fixed ω by solving the cranking Hartree – Fock – Bogolyubov equations. The solutions provide the angular momentum and energy relative to the non – rotating state with ω = 0. The deformation lattice is transformed into Cartesian coordinates, X = $\beta_2\cos(\gamma + 30^\circ)$ and Y = $\beta_2\sin(\gamma + 30^\circ)$, and 9 x 11 points in the (X, Y) plane, starting from X = 0.05 and Y = -0.20. The calculations have been performed at four different hexadecapole deformations with step of 0.04. The minimization was performed in the way that for a fixed configuration the total routhian was first minimized at each (β_2, γ) grid point with respect to β_4 and in a second step the equilibrium deformation was obtained by minimizing over the whole grid. The calculations have been performed for 18 different rotational frequencies, starting from $\hbar\omega$ = 0.05 MeV with a step length of 0.04 MeV.

The pairing gap Δ_0 is calculated self – consistently at each grid point for ω = 0 and then allowed to decrease with ω as:

$$\Delta_{\omega} = \Delta_0\left(1 - \frac{1}{2}\left(\frac{\omega}{\omega_c}\right)^2\right) \qquad (\omega < \omega_c) \qquad (2.32)$$

and

$$\Delta_{\omega} = \Delta_0\frac{1}{2}\left(\frac{\omega}{\omega_c}\right)^2 \qquad (\omega > \omega_c) \qquad (2.33)$$

10

The critical frequency ω_c, where Δ reaches half of its original values Δ_0, was for even nuclei chosen to be 0.4 MeV for neutrons and 0.5 MeV for protons. In order to incorporate blocking effects in the calculations, the critical frequency was increased by 0.1 MeV for odd particle numbers and Δ_0 was multiplied by a factor of 0.85. The chemical potential λ_n and λ_p were adjusted separately at each frequency in order to give the correct expectation value of the number of nucleons [Gue99].
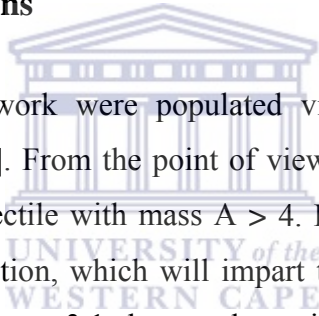
CHAPTER 3

EXPERIMENTAL TECHNIQUES AND EQUIPMENT

This chapter will deal with the study of a nucleus at high angular momentum. We shall examine the formation of high spin states via the mechanism of fusion – evaporation reactions and look at some of the ways of analyzing the spectroscopic information gained in such pursuits in order to characterize the different nuclear structures observed in the decay of high spin states.

3.1 Nuclear reactions

3.1.1 Heavy – ion reactions

The nuclei studied in this work were populated via the heavy – ion fusion – evaporation reactions [Boh36]. From the point of view of nuclear reactions, a heavy ion is defined to be any projectile with mass A > 4. For one to study the high spin states, one will require a reaction, which will impart the largest angular momentum into the nucleus of interest. Figure 3.1 shows schematically different types of nuclear reactions depending on the value of the impact parameter, b. Accelerators devoted to the study of heavy-ion reactions can produce beams of ions up to ^{238}U, at typical energies of 1-10 MeV per nucleon, although much higher energies are also possible. At large impact parameters, Coulomb effect dominates, and Rutherford scattering or Coulomb excitation may occur as shown in Figure 3.1. Fusion – evaporation reactions are the best way of producing experimentally high spin states with large cross – sections. In a fusion – evaporation reaction, the kinetic energy of the collision in the centre of mass frame is converted into an excitation energy of the compound system. When the nuclear densities of the target and the projectile just begin to overlap, nuclear reactions can occur. At such small overlaps ordinary elastic or inelastic scattering and few-nucleon transfer through direct reaction may occur. If the impact parameter is small enough such that the nuclei can overlap completely, a compound nucleus, representing a complete fusion of the two nuclei, can form as an intermediate

state. However, to overcome the repulsive Coulomb barrier, the incident ion must be energetic, and thus the compound nucleus is formed with considerable excitation energy [Reg00]. The amount of angular momentum transferred into the compound nucleus is given by b × p where b is the impact parameter and p is the linear momentum, *mv*, of the projectile.
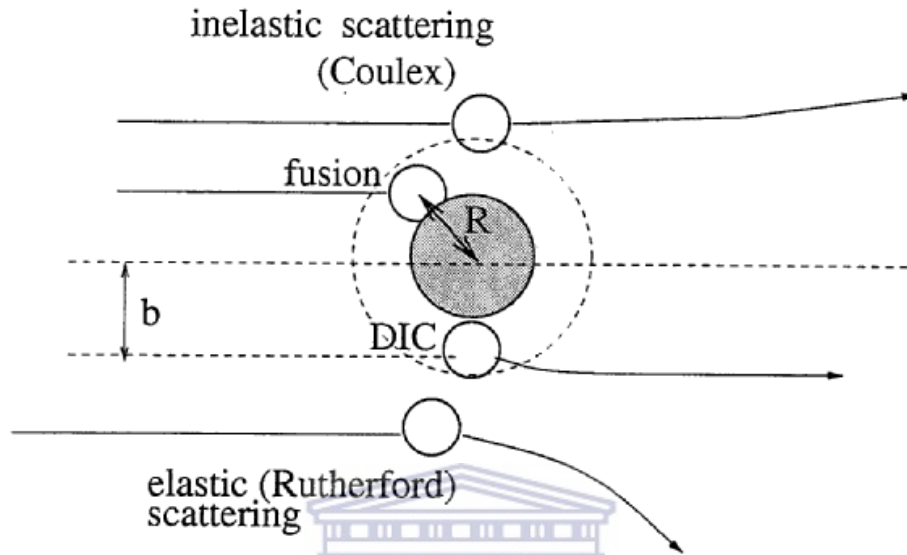
Figure 3-1: When projectile energies are large enough to penetrate the Coulomb barrier various types of the heavy – ion collisions as a function of the impact parameter occur [Reg00].

The angular momentum transferred is simply ℓ = mvb. Thus, the higher energy of the beam particles, the more angular momentum will be transfered into the compound system. It should be noted as Figure 3.1 shows, fusion reactions only occur for small values of the impact parameter, while other nuclear reactions occur at increased values of b.

Once the excited compound state is formed, there are many channels available for its decay. It can split more-or-less in half in a fission process. For heavier nuclei, the study of fission mode provides a check on theories derived from the study of more familiar cases of transuranic fission. For lighter nuclei a more probable range of decay of the compound nucleus is through particle emission, for fission is inhibited by substantial Coulomb barrier. In reactions with heavy nuclei the compound nucleus is extremely proton rich, but the preferred decay mode is still neutron emission. This remains so, even for heavy nuclei with proton excess of 10 - 20 or more. It is thus possible to study nuclei far from stability on the proton-rich side through (HI, xn)

reactions, where HI indicates any heavy ion and x may be in the range 5 - 10. Another unique feature of heavy-ion reactions is the transfer of large amounts of angular momentum to the compound nucleus. For example, in the reaction ^{40}Ca + ^{197}Au, the Coulomb barrier is about 200 MeV. If we use 200 MeV incidents ^{40}Ca, a grazing collision will provide about 140 ℏ of angular momentum to the system.
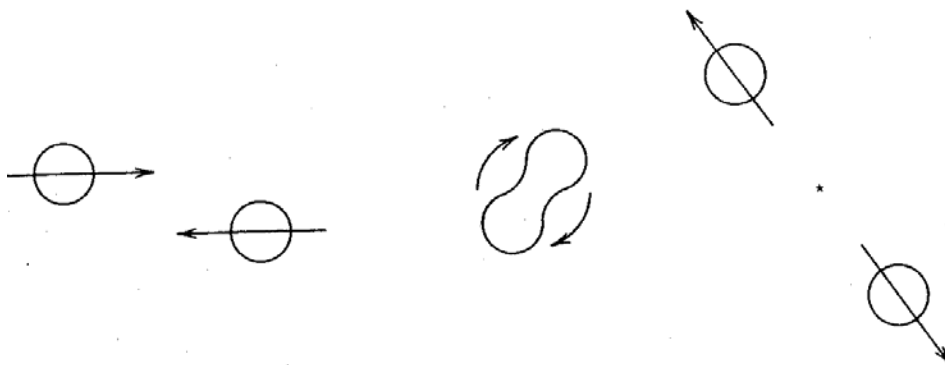
Figure 3-2: In nuclear molecule formation, there is not quite complete fusion of the two particles; they retain a "memory" of their previous character and break apart accordingly. The internal energy of the system can show rotational and vibrational structures, just like an ordinary molecule. From Ref [Kra88].

Even at collisions with smaller impact parameter, it would not be unusual to transfer an angular momentum of $\ell \geq 40$ ℏ to the compound system. At such rotational frequencies, the nuclear force may not be able to provide the necessary centripetal acceleration, and the compound system may be completely unstable and therefore unable to form. In such a case, a new type of system is possible, called a nuclear molecule. The two nuclei do not form a compound system, corresponding to complete sharing of incident energy. Instead a system analogous to a diatomic molecule is formed, exists for a short time, and then breaks apart in the same initial configuration, as shown in Figure 3.2. Because the decay occurs into the original particles, the combine system retains a considerable "memory" of its formation, contrary to the basic assumption of the compound-nucleus model. Evidence for such molecular states comes from observing the rotational and vibrational excitations that correspond closely with those in ordinary molecules. Resonance in the cross section corresponds to the vibration states permitted in the molecular system.

In heavier nuclei, highly excited states with $\ell \geq 40$ - 50 ℏ can be populated in the compound system. The emission of a few neutrons from the excited compound nucleus can change the angular momentum only little (a 5 – MeV neutron carries at

most only ℓ~3 ℏ), and following the neutron emission, excited bound state can be formed with angular momentum quantum number of 40 or so [Kra88].

3.1.2 Complete fusion reactions

Nuclear fusion is a process where two or more nuclei combine to form an element with a higher atomic number (more protons in the nucleus). Fusion is the reverse process of nuclear fission. An example of a fusion reaction for deuterium − tritium reaction is shown in Figure 3.3.
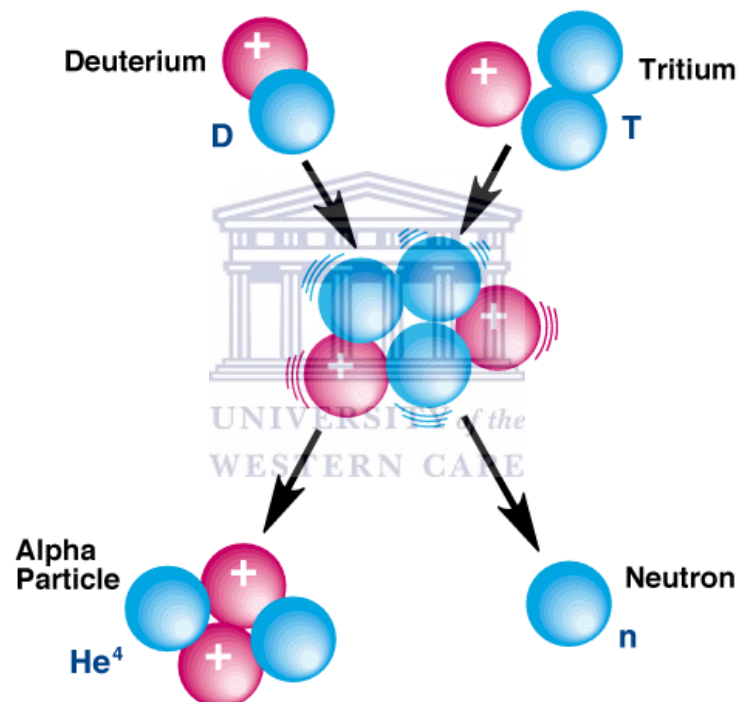
Figure 3-3: The deuterium – tritium fusion reaction is the most efficient reaction known in terms of energy released [Hae82].

In fusion reactions there is energy released and this energy is related to the Einstein's famous equation, $(E = mc^2)$. Heavy − ion fusion followed by neutron evaporation (complete fusion reactions) have become, in the last decades, the primary means of producing nuclei at high − excitation energy and spin, for spectroscopic studies with γ - rays. By simple choice of beam energy and target - projectile combination very wide range of nuclei can be reached, in many cases with considerable selectivity. A

limitation, however, is that with stable beams and targets essentially only neutron – deficient products are accessible. For stable and neutron rich isotopes, information about the structure at high spin is generally deduced from α – induced reactions, Coulomb excitation (only in the case of stable isotopes), deep – inelastic or fusion – fission reactions [Wil82]. A schematic incomplete fusion reaction also called a massive transfer is illustrated in Figure 3.4. It may be described in the following manner. The projectile does not completely fuse with the target nucleus, but breaks up into two fragments. One fragment fuses with the target nucleus, resulting in the formation of the final reaction product (residual nucleus), after evaporation of some neutrons.
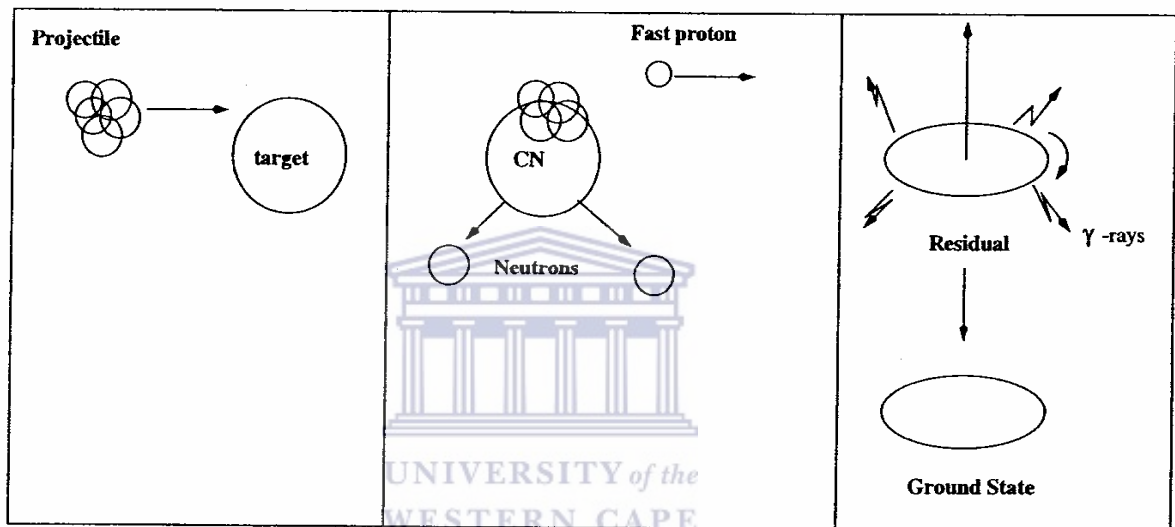
Figure 3-4: An example of a massive transfer nuclear reaction between a projectile and a target nucleus. From Ref. [Vym03].

The other fragment (an α - particles or proton) moves away without interacting and with unchanged velocity [Jun03]. It is known that the incomplete fusion mechanism populates high – spin states with relatively high cross sections. With the advent of multiple – elements particle – detector systems and arrays of γ - rays detectors, selection of such reaction channels has been facilitated [Dra97].

3.1.3 Elastic scattering and direct reactions

At low and moderate bombarding energies Coulomb force plays an important role in determining the course of heavy-ion collision. This is illustrated schematically in

Figure 3.5, which shows the effect on several trajectories near a target nucleus. Those with large impact parameters (1 and 2) miss the nucleus altogether and the particles are deflected away by Coulomb field. For a grazing collision (path 3), the projectile just reaches the target and direct nuclear reactions begin to take place. At small impact parameters (path 4), the projectile collides with the target well inside the interaction radius and more complex reactions, sometimes leading to fusion, predominate. The observed behavior of heavy-ion elastic scattering is broadly in accord with this classical interpretation. Small scattering angles correspond to trajectories with large impact parameters.
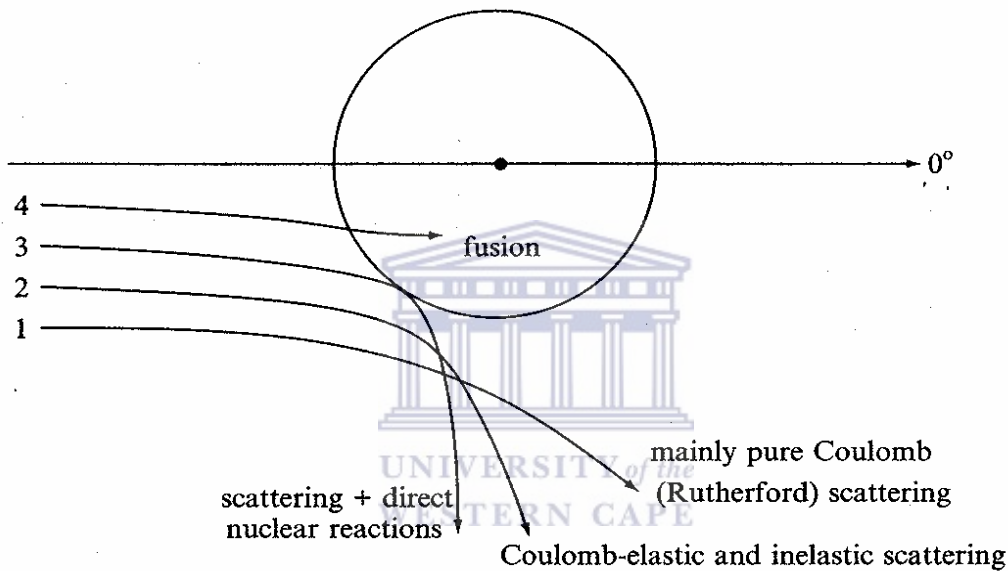
Figure 3-5: Effect of Coulomb repulsion on different trajectories in a heavy – ion collision. Trajectories 1 and 2 miss the nucleus and are scattered by the Coulomb field. Coulomb-inelastic excitation can also occur. On trajectory 3, the projectile grazes the nucleus during which simple, direct nuclear reactions can take place (as well as elastic and Coulomb-inelastic scattering). The projectile on trajectory 4 is shown entering the target nucleus and fusing with it. From Ref. [Lil92].

These do not reach the nuclear surface, and the cross section σ (θ) follows the Rutherford formula σ_{Ruth} (θ) up to a certain angle. Beyond this point, σ (θ) falls below σ_{Ruth} (θ), because trajectories with smaller impact parameters, which would be scattered by a point charge to larger angles, interact with target nucleus, and the onset of nuclear reactions begins to remove flux from the elastic channel. Larger angles correspond to more intimate contact, which leads to greater flux loss and a rapidly falling cross section. If the heavy ion is not too massive, i.e. if its wavelength is not

comparable with its size, oscillations may be seen to superimpose on an otherwise classical distribution.

They are due to diffraction of the projectile wave by the surface of the target nucleus acting as a single, absorbing edge. When a heavy ion passes close to the target (path 2), the impulse due to the Coulomb force acting between the particles can be strong enough to lead to a significant amount of inelastic excitation, known as Coulomb excitation (or coulex) [Lil92].

3.1.4   Deep inelastic reactions and limits to fusion

When two heavy nuclei collide and the orbital angular momentum exceeds a critical value (L_c,) a complex sequence of reaction processes can take place. Figure 3.6 illustrates the progress of such a collision. As the nuclei approach each other, a significant part of their relative kinetic energy is converted into Coulomb potential energy.
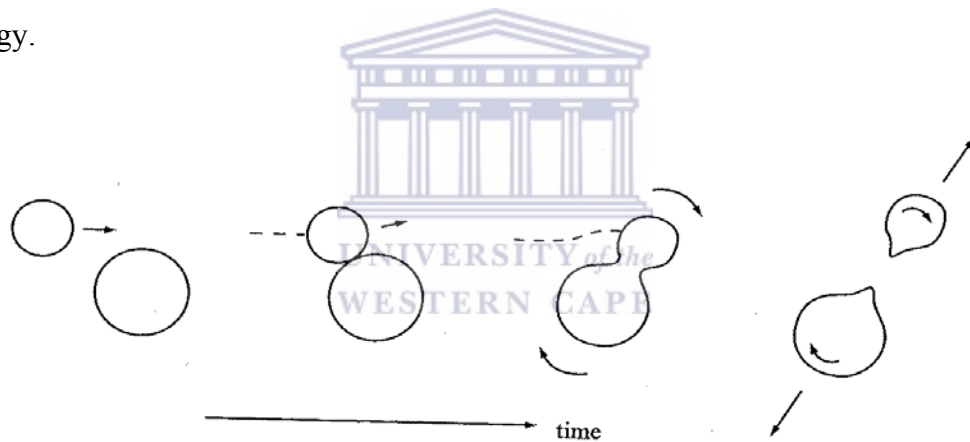
Figure 3-6: Sequences in the progress of a collision between the two nuclei when the angular momentum is greater than can be sustained by the combined system. From Ref. [Lil92].

This means that they may be moving slowly enough so that, during the period of contact as they pass each other, there is enough time for a large amount of the remaining relative kinetic energy to be converted into internal excitation. This energy dissipation occurs via nucleon-nucleon collisions and mass exchange through the region of contact, where a neck of nuclear matter may form as the two nuclei stick together and begin to rotate as a single unit. The angular momentum is too great for fusion to occur and, a short time later, the fragments separate with a certain amount of kinetic energy corresponding to their relative angular momentum. They then acquire

a considerable amount of extra, radial kinetic energy from their mutual Coulomb potential energy as they repel each other. During contact, nucleon transfer occurs in both directions, and the masses and charges of the final products may not be very different from those of the initial reactants. However, contact time does not last long enough for a complete rotation of the combination to take place and the angular distribution is peaked in the forward direction, characteristic of a direct reaction. Such highly dissipative reactions, often referred to as deep-inelastic reactions, are intermediate between simple direct and true compound-nuclear reactions. They become increasingly important in collisions with heavier projectile, which for a given energy, bring more angular momentum into the combined system [Lil92].

3.1.5 Decay of the compound nucleus

The compound nucleus is formed in a state of extreme excitation. For the reactions used in this work, the compound nucleus typically has excitation energy of around 40 MeV, with a maximum angular momentum of around $25 - 35$ ℏ. The compound nucleus loses this excitation energy in various ways, shown schematically for a four-neutron evaporation channel in Figure 3.7. This is due to the fact that the nucleus is no longer stable against the centrifugal repulsion. If the compound nucleus does not undergo fission, the majority of the excitation energy is removed by particle emission (protons, neutrons, alpha particles). Charged particle evaporation (protons, alpha particles) is normally suppressed by the Coulomb barrier, and neutron evaporation forms a large part of the fusion-evaporation cross section. The evaporation of particles carries away large amounts of excitation energy (at least $8 - 10$ MeV), but a small amount of angular momentum. Thus the evaporation of particles gives a steep descent towards the ground state, as shown in Figure 3.7. When the excitation energy is below the particle evaporation threshold (approximately 8 MeV above the yrast line) the nucleus continues to de-excite through γ-ray emission. The nucleus is still relatively excited, and decays by emission of statistical or cooling γ-rays. These are usually high-energy dipole transitions, carrying away large amounts of excitation energy, but again very little angular momentum. These γ-rays are normally not detected in a γ-ray spectroscopy experiment. As the cooled nucleus approaches the yrast region, γ-

19

ray emission proceeds through transitions of lower energy, carrying more angular momentum, to the ground state.
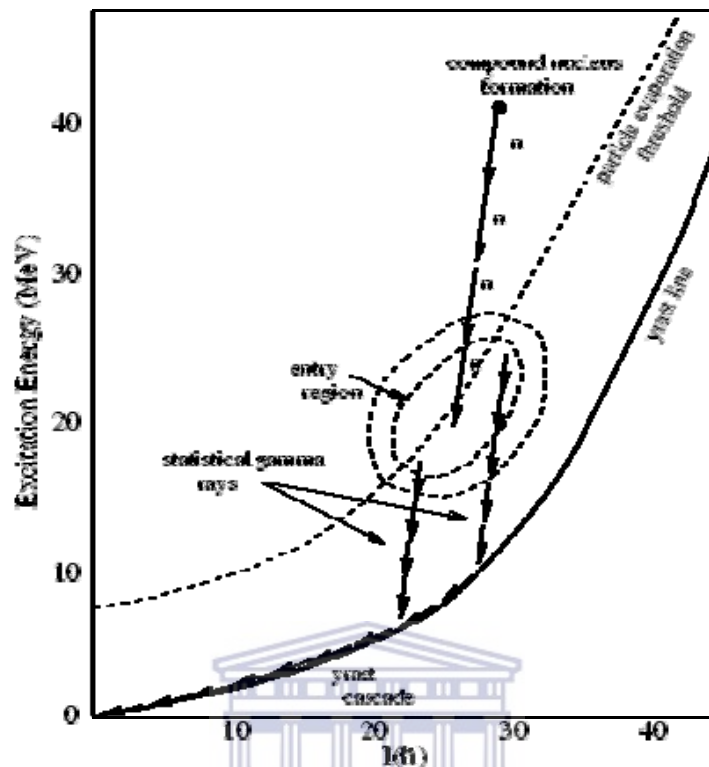
Figure 3-7: A schematic of the decay of the compound nucleus. In this example, four neutrons are first emitted, carrying away a large amount of excitation energy, but little angular momentum. Below the particle evaporation threshold, de-excitation continues to the ground state through γ - ray emission [Gre99].

It is these *yrast-like* transitions that are of particular interest to the γ - ray spectroscopist, since they carry enough intensity to be isolated in a γ - ray spectrum, and can reveal the properties of the nucleus being studied.

3.2   Interaction of gamma – rays with matter

The interaction of gamma rays with matter is markedly different from that of charged particles. Gamma rays and X-rays, which are both electromagnetic radiation, show a characteristic exponential absorption in matter and have no definite range such as that found for electrons or alpha particles.

Three processes are mainly responsible for the interaction of gamma rays with matter:

(1) Photoelectric absorption, (2) Compton scattering by the electrons in the atoms, and (3) pair production - the creation of electron-position pairs as the result of the interaction between gamma rays and the electric fields of atomic nuclei. For the purposes of this work, photonuclear and other such small effects are neglected. The three main processes shown in the Figure 3.8 are discussed below.
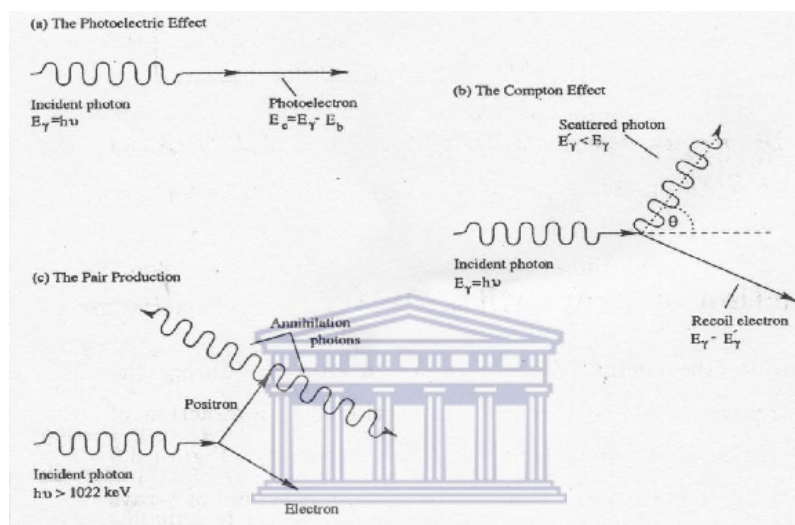
Figure 3-8: Shows the three main processes that occur when the gamma – rays interact with matter.

3.2.1 Photoelectric effect

In the photoelectric effect, the photon imparts all its energy to an electron in an atom of the absorbing material, giving the electron a kinetic energy equal to the original energy of the photon minus the binding energy of the electron. The process of photoelectric absorption is shown in Figure 3.9. An incident photon is completely absorbed by an atom in the absorber material, and one of the atomic electrons is ejected. This ejected electron is known as a photoelectron. The electron must be bound to the atom, to give conserved energy and momentum. This type of interaction is most probable for a gamma ray with energy just in excess of the binding energy of the electron. Photoelectric absorption occurs in the vicinity of an atom where the photon's energy is wholly converted into releasing an electron from its site in the

material. The atom which has lost the electron may deexcite by releasing other less tightly bound electrons.
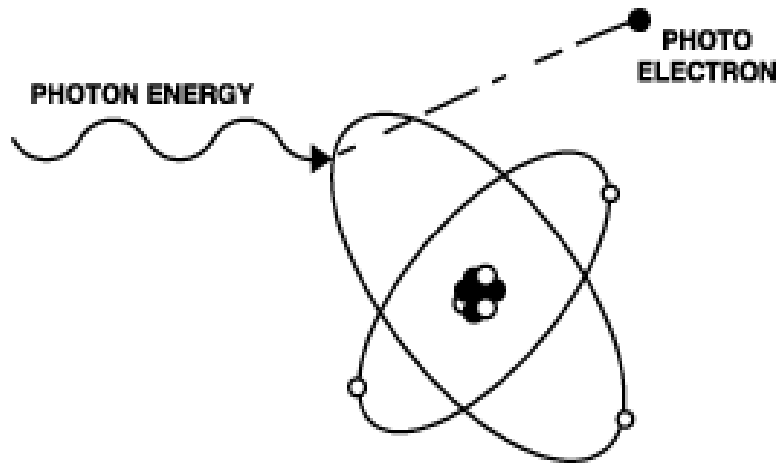
Figure 3-9: Shows the process of photoelectric absorption.

Electrons emitted by this process are called Auger electrons. Alternatively, an electron from the higher shell may fill the vacancy in the inner shell with the emission of a characteristic X-ray photon. This is known as X-ray fluorescence. This X-ray in turn may interact and be absorbed by the medium. Photoelectric absorption is the most favorable process for the γ - rays spectroscopist, since the incident photon deposits all of its energy into the detector or medium, but it is only dominant for low energy photons (< 200 keV).

The photoelectron emerges with kinetic energy given by:

$$T_e = E_\gamma - B_e \qquad (3.1)$$

where B_e is the binding energy of the atomic electron.

The interaction is dependent upon Z, and an approximate expression for the absorption probability τ is given by:

$$\tau \propto \frac{Z^n}{E_\gamma^{3.5}} \qquad (3.2)$$

Here n is normally between 4 and 5 depending on the absorber material. This dependence on Z explains the choice of high - Z materials such as lead for shielding purposes. The photoelectric mass attenuation coefficient (μ_m) varies strongly with E_γ

and Z, as shown in Figure 3.10. The sharp rise at energy of about 90 keV for lead is due to the added contribution of the innermost, K-shell, since in lead the K electron has a binding energy B_k of 88 keV. Below this energy, the K electrons do not contribute to the photoelectric absorption because there is not enough energy to eject them from the atom. The discontinuity in the energy dependence of μ_m is known as the K edge. The energy of the K edge is approximately proportional to Z^2. At lower photon energies, photoelectric absorption edges due to less bound shells (L, M…) become evident. Note that the relative contribution of the two K electrons is much greater than that of all the rest of the electrons in the lead atom put together. This is at first surprising since they occupy only a relatively small fraction of the atom's volume. However, the need to conserve both energy and momentum forbids the photoelectric effect from occurring on a free electron.
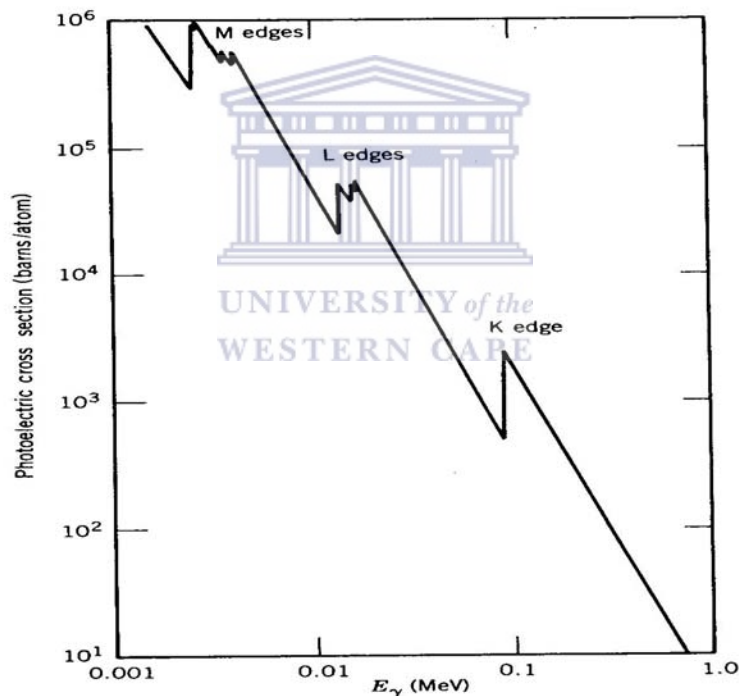
Figure 3-10: Photoelectric cross section in Pb. The discrete jumps correspond to the binding energies of various shells. The K – electron binding energy, for example, is 88 keV for Pb. To convert the cross section to the linear absorption coefficient τ in cm^{-1}, multiply by 0.033. From Ref. [Kra88].

The process must take place in the vicinity of an atom, which takes away the excess momentum but, because of its much greater mass, acquires very little of the original energy. The smaller the electron's binding energy relative to E_γ the more it appears

23

like a free electron and the smaller will be the probability of the photoelectric absorption (for $E_\gamma > B_k$) [Kra88].

3.2.2 Compton scattering

In the Compton effect the photon imparts a portion of its energy to electron and is deflected in the process. In this case, an incident γ - ray scatters from an outer shell electron in the absorber material at an angle θ, and some of the γ - ray energy is imparted to the electron. The process is illustrated schematically in Figure 3.11.
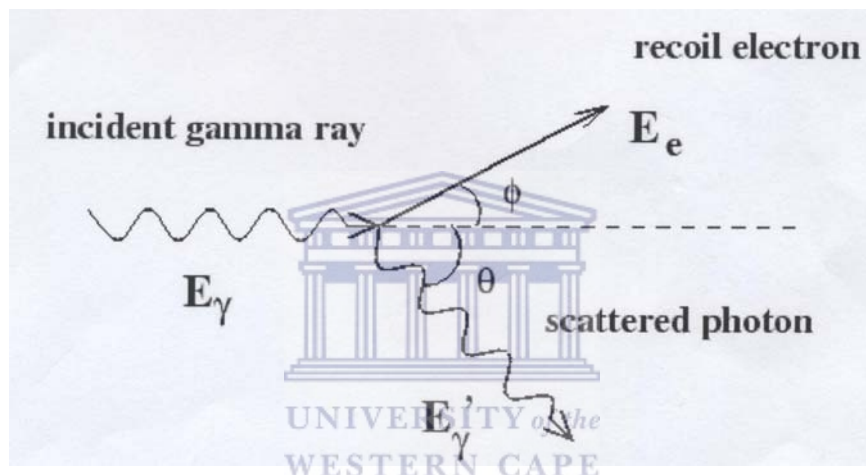
Figure 3-11: The process of Compton scattering.

Conservation of energy and momentum leads us to the following expression for the energy of the scattered photon:

$$E_\gamma^{'} = \frac{E_\gamma}{1 + \left(\dfrac{E_\gamma}{m_0 c^2}\right)(1 - \cos\theta)} \tag{3.3}$$

where E_γ is the incident photon energy, $E_\gamma^{'}$ is the energy of the scattered photon, θ is the scattering angle and $m_0 c^2$ is the electron rest mass energy. The kinetic energy of the electron after the collision is given by:

$$T_e = E_\gamma - E_\gamma^{'} = \frac{E_\gamma^2 (1 - \cos\theta)}{m_0 c^2 + E_\gamma (1 - \cos\theta)} \tag{3.4}$$

It can be seen that, since all scattering angles are possible, the electron energy ranges from zero for $\theta = 0^\circ$ to $\dfrac{2E_\gamma^2}{\left(m_0 c^2 + 2E_\gamma\right)}$ for $\theta = 180^\circ$, and that the photon never loses the whole of its energy in any one collision. The scattered photon can then continue through the absorber and interact again or scatter out of the absorber material completely.

This process, where the scattered photon escapes, is very important for the γ - ray spectroscopist. If the full energy of the incident photon is not absorbed in the detector, then there is a continuous background in the energy spectrum, known as the Compton continuum. This continuum extends up to an energy corresponding to the maximum energy transfer in a single interaction, where there is a sharp cut-off point, known as the Compton edge. Compton scattering is the most probable process for photons in the intermediate energy range and the probability decreases rapidly with increasing energy. The probability is also dependent on the number of electrons available for the photon to scatter from, and hence increases with increasing Z.

3.2.3 Pair production

The third important γ - ray interaction is the process of pair production, shown in Figure 3.12. This process is effective at high energies (> 1.022 MeV).
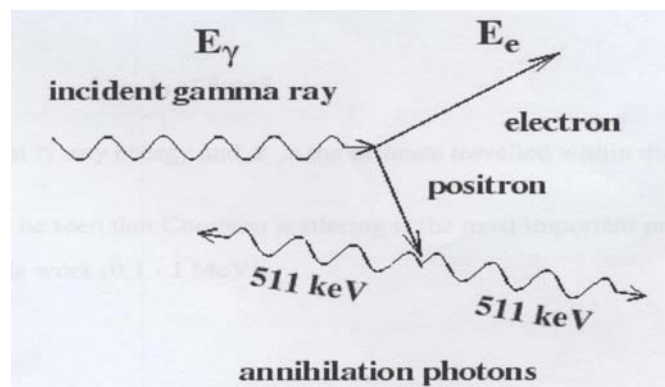
Figure 3-12: The process of pair production

In pair production, the photon disappears and a pair of electron and positron is created. Since the total rest mass energy of the electron and positron is $2m_e c^2 = 1.022$ MeV, this effect does not occur unless the photon has at least this much energy.

25

Above this threshold energy, the probability for pair production increases steadily with increasing energy. The total kinetic energy of the electron - positron pair is equal to the energy of the photon less 1.022 MeV. Once formed, these electron and positron move about and lose energy as a result of collisions with atoms in the surrounding medium. After the positron has slowed down to very low energies it combines with an electron, the two particles disappear, and two photons are produced (annihilation radiation) each having energy of 0. 511 MeV. In this process, the entire photon energy is converted in the field of an atom into the creation of an electron –positron pair with total kinetic energy given by:

$$T_- + T_+ = E - 2mc^2 \qquad\qquad (3.5)$$
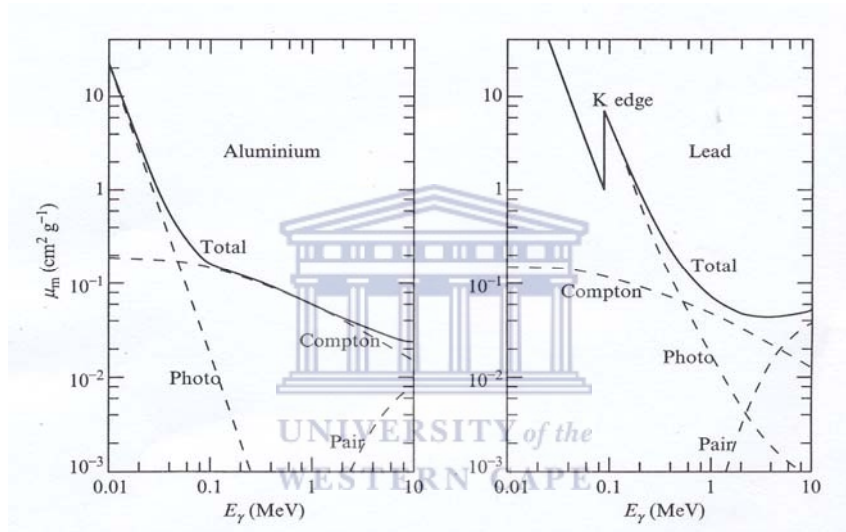
Figure 3-13: Photon mass – attenuation coefficients for aluminum and lead as a function of photon energy. Dashed lines show the separate contributions due to the photoelectric effect, Compton scattering and pair production. From Ref. [Lil92].

Like the photoelectric effect, pair production requires the presence of a heavy body in order to conserve both energy and momentum. This means that there is some dependence of its probability on Z, as can be seen by comparing pair production for Al and Pb, as shown in the Figure 3.13.

3.2.2 Attenuation

All three interaction processes described above cause a photon beam to be attenuated as it passes through matter. Photons which undergo photoelectric absorption or pair

production disappear altogether and most of those that are Compton scattered are deflected away from reaching a detector placed in the forward direction. The dependence of photon intensity on absorber thickness is most easily calculated for a well –collimated beam. Consider a beam, of intensity I photons per second, incident on a thin section (thickness dx) in a slab of material whose atomic density is of N. If the total interaction cross section per atom of material is σ, the rate of removal of photons from the beam is given by:

$$dI = - N\sigma I \, dx \hspace{3cm} (3.7)$$

The total cross section has contributions from all three-interaction processes.

$$\sigma = \sigma_{pe} + Z\sigma_c + \sigma_{pp} \hspace{3cm} (3.8)$$

where σ_{pe} and σ_{pp} are the atomic photoelectric and pair production cross-section, respectively, and σ_c is the Compton scattering cross section for a single electron as shown in Figure 3.13, [Lil92].

3.3 Experimental equipment

For one to study high – spin states in nuclei, the following equipment is needed:
(i) A suitable reaction to populate the nuclei of interest with sufficient reaction rates.
(ii) Accelerator to produce the desired accelerated projectile particle and beam line to deliver the beam to the target in the vault.
(iii) Detectors with high γ - ray efficiency and good resolution

3.3.1 An overview of the facilities at iThemba LABS

iThemba Laboratory for Accelerator Based Science is situated in Faure just 30 km away from Cape Town. A floor – plan is shown in Figure 3.14. Currently there are two large accelerators in operation at iThemba LABS namely a Van de Graaff and Separated – Sector – Cyclotron (SSC) accelerators.
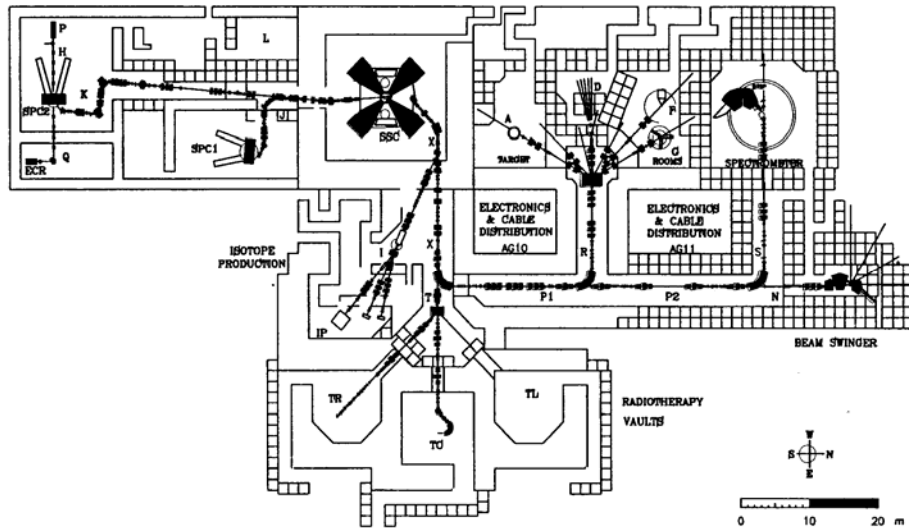
Figure 3-14: An overview floor – plan of the facilities at iThemba LABS.
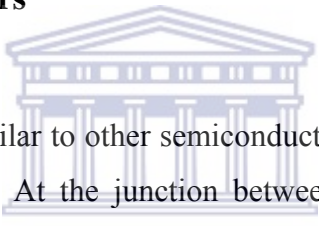
Table 3.1: Abbreviations and descriptions used on the plan – view shown in Figure 3.14.

Abbreviation	Description
A	Scattering chamber beam line
D	Collimated neutron beam facility
ECR	Electron Cyclotron Resonance (ECR) ion source
ECD	Electronic and cable distribution
F	High-energy gamma-ray detectors (AFRODITE array)
G	Gamma-ray angular correlation table
IP	Isotope production facility
L	Low-energy experimental area
P	Polarised-ion source
SPC1	Solid-pole injector cyclotron for light ions
SPC2	Solid-ion cyclotron for heavy and polarized ions
SSC	Separated-Sector Cyclotron
TC	Isocentric system for neutron therapy
TR	Horizontal beam line for proton therapy
TL	Beam lines for proton

The Van de Graaff accelerator is mostly used to study material science. The SSC accelerator is mostly used in radiotherapy to treat cancer patients and to manufacture radioisotopes. These isotopes are used in nuclear medicine and in agriculture

products. The two solid – pole injector cyclotrons are shown in Figure 3.14. These are the K = 8 (SPC1) [Dut 87] used to accelerate light – ion and the K = 10 (SPC2) for heavy – ion and polarized hydrogen ion beams [Bot87]. The beam is extracted from the injector cyclotron and then further accelerated in the SSC until the beam particles attain the required kinetic energy. From the SSC the ions are guided to the experimental vault via the high – energy beam line using quadrupole magnets for focusing and dipole for bending the beam. The SSC delivers a pulse beam with a repetition rate from 8 to 26 MHz. Furthermore a wide variety of beams are available including light and heavy – ions. The K = 200 Separated – Sector – Cyclotron (SSC) [Bot87a] of the dimensions 13.2 m in diameter and 7 m in height has four sector magnets. The time allocation for physics experiments is over the weekend. Typically the beam is available from 18h00 on Friday afternoon to 05h00 Monday morning.

3.3.2 Germanium detectors

The germanium detectors, similar to other semiconductor detectors, are large reverse-biased p - n junction diodes. At the junction between the p – type and n – type material, the migration of electrons from the n – type material and holes from the p – type material gives rise to a region of net zero charge. In gamma ray experiments, the germanium detectors used have the n contact on the inside and the p contact on the outside. The reason for this is that the n contact is much thicker than the p contact and may attenuate the incident radiation. The net positive charge on one side of the junction, and the net negative charge on the other side, set up an electric field gradient across the depletion region. Any gamma rays interacting with the germanium will produce electron – hole pair in the depletion region, which will then be swept to the edges of the detector because of the electric field gradient, constructing an electric current. This electric current is then collected by the pre – amplifier that is host inside the detector cryostat. The energy required for creating an electron – hole pair in Ge is approximately 3 eV. Germanium detectors are best operated at liquid nitrogen temperature to reduce the leakage current and to increase the mobility of the charge carriers. Typical operating voltages may be 1000 V to 3000 V applied across only a few centimeters of germanium [Gil95]. At iThemba LABS we use two types of Ge

detectors, which are clovers and LEPS detectors and they are going to be discussed in the next sections.

3.3.2.1 Clover detectors

Clover detectors are ideal for detecting high-energy gamma rays because of their high efficiency in the add - back mode. The clover detector is shown in Figure 3.15.

Figure 3-15: A Clover detector showing the tapered rectangular cryostat and a cylindrical liquid nitrogen (LN2) dewar.

These detectors are composite detectors. A composite detector is made up of several Ge crystals packed closely together in the same cryostat. In this way a large detector can be created with high photopeak efficiency and high resolving power, since the (small) individual crystals minimize the effect of the Doppler broadening. An array of such detectors has a high granularity and high efficiency. Clover detectors consist of four n - type coaxial HPGe crystals with a spacing of about 0.2 mm [Jon95] as shown in Figure 3.16. The crystals with the dimensions of 70 mm in length, 50 mm in diameter, 36 mm tapering length and 41 mm side of the crystal surface are packed in a

common cryostat. Changing the shape of the crystal can further increase the active volume of an HPGe detector. If the crystal is bulletined (has the corners rounded off), then the electric field inside will be more uniform allowing active volumes of approximately 400 cm^3 to be achieved.
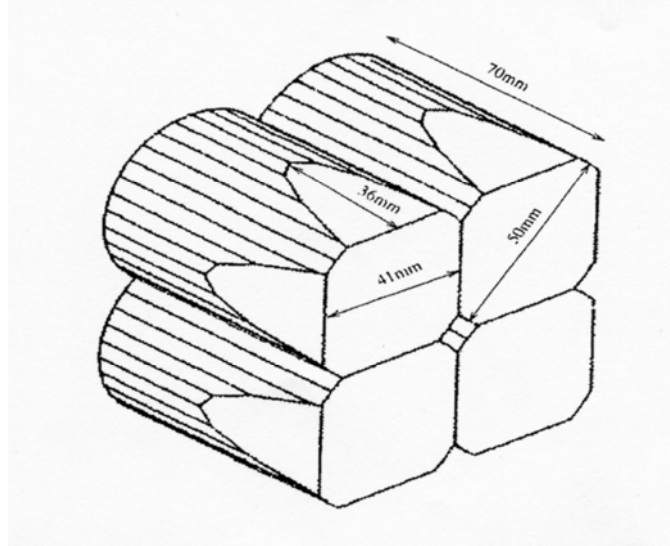
Figure 3-16: The segmented clover germanium detector crystal and how are they packed inside the detector. A clover detector consists of four n - type coaxial HPGe crystals.

The clover detectors have large efficiency for high energy γ - rays. The granularity of the clover detectors leads to a decreased Doppler broadening of the peaks and allows a possibility for the reconstruction of the total γ - energy by adding up energies deposited in more crystals due to Compton scattering (add-back), which thus increases the photo peak efficiency. The clover detectors are coupled to an automatic LN_2 filling system, which tops up the dewars with LN_2 from a storage tank every 12 hours.

Some technical specifications of the AFRODITE array for clovers:

- The distance from the crystal surface to the target center, D_{tc} = 196 mm.
- The distance from the detector end-cap to the crystal surface, D_{ec} = 20 mm.
- The total opening angle, T_{ang} = 23.2°
- The solid angle per detector, S_{ang} = 1.34% of 4π (for a distance of 0.2 mm between crystals and S_{ang} = 16.8°).

The clover detectors are each housed in a Compton suppression shield that is made of bismuth germinate (BGO), which is a highly efficient scintillator for the detection of γ - rays [Em186, Lie84]. Figure 3.17 shows the schematics of a Ge detector and also shows BGO shield.
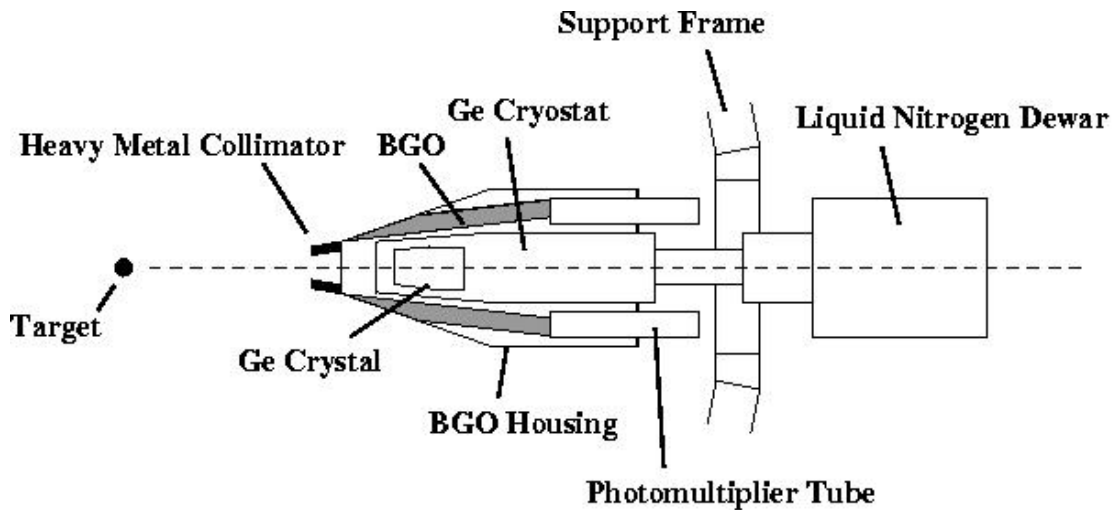
Figure 3-17: A Ge detector with tapered rectangular cryostat and a cylindrical liquid nitrogen dewar (LN$_2$) and covered with a BGO shield.
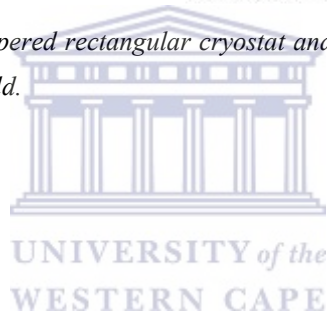
3.3.2.2 LEPS detectors

LEPS are planar detectors made of a single crystal of p - type HPGe, electrically segmented into four quadrants, with the dimensions of 10 mm thick and 60 mm in diameter. The signal from each quadrant is processed separately, as in the case of the clovers. The LEPS detectors are efficient in detecting low energy (between 30 and 300 keV) γ - rays. The LEPS detectors dewars are filled with LN$_2$ from the storage tank every 24 hours.

Some technical specifications of the AFRODITE array for LEPS:

- The distance from crystal surface to the target center, D_{tc} = 119 mm for a 4 mm gap between the target chamber and the end – cap.
- The distance from the detector end – cap to the crystal surface, D_{ec} = 15 mm.
- The total opening angle, T_{ang} = 28.3^o.
- The solid angle per detector, S_{ang} = 1.57 % 4π and S_{ang} = 19.7^o

3.3.3 Compton suppression

Because of the Compton scattering interaction many gamma rays, which enter the Ge detector, will not deposit their full energy, leading to a large Compton continuum. In order to reduce the contribution of scattered gamma rays the Ge detector can be surrounded by an inorganic scintillator detector. The majority of escape suppression shields use bismuth germinate Bi_4GeO_{12} (BGO).
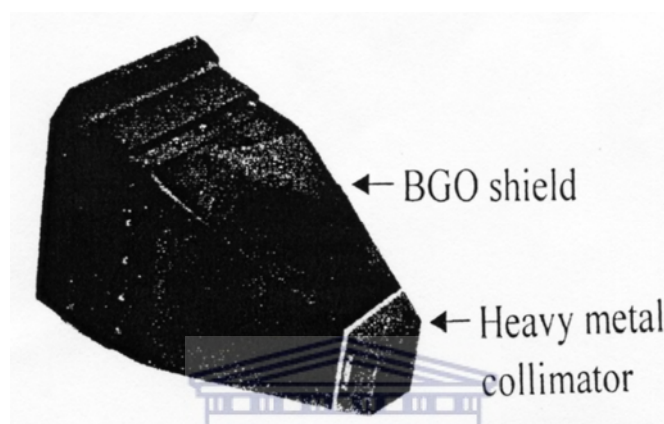
Figure 3-18: A BGO Compton suppression shield specifically designed to house a standard clover detector and showing the tapered heavy metal collimator with a 35 mm by 35 mm entrance window for γ - rays at the front end.

The reason for this choice is that BGO has excellent timing properties, which are desirable for coincidence work, and high density (7.3 g/cm^3), so that a relatively small amount of material is needed in order to stop fully the scattered photons. The BGO Compton suppression shields with the dimension of $\approx$ 26 cm in length, one of which is shown in Figure 3.18, are essential in reducing the unwanted background from Compton scattered γ - rays. The BGO shields are used to reject those gamma rays, which deposit only part of their energy in the Ge before scattering out of the detector. The percentage of gamma rays that scatter out is energy dependent, but typically only ~ 65 % deposit their full energy in a single Ge detector. The Compton suppression factor (CSF) [Em186, Sha88], or the background reduction, is obtained by taking the ratio of the unsuppressed to the suppressed spectrum. For the energy range of 300 – 1000 keV, the CSF is obtained to be about 3.33 for a Ge detector [Keė00]. Suppressed and unsuppressed spectra were obtained with a ^{60}Co radioactive source as shown in

Figure 3.19. Each BGO Compton suppression shield consists of 8 optically separated segments, each of which has in turn 2 PM (Photo Multiplier) tubes.
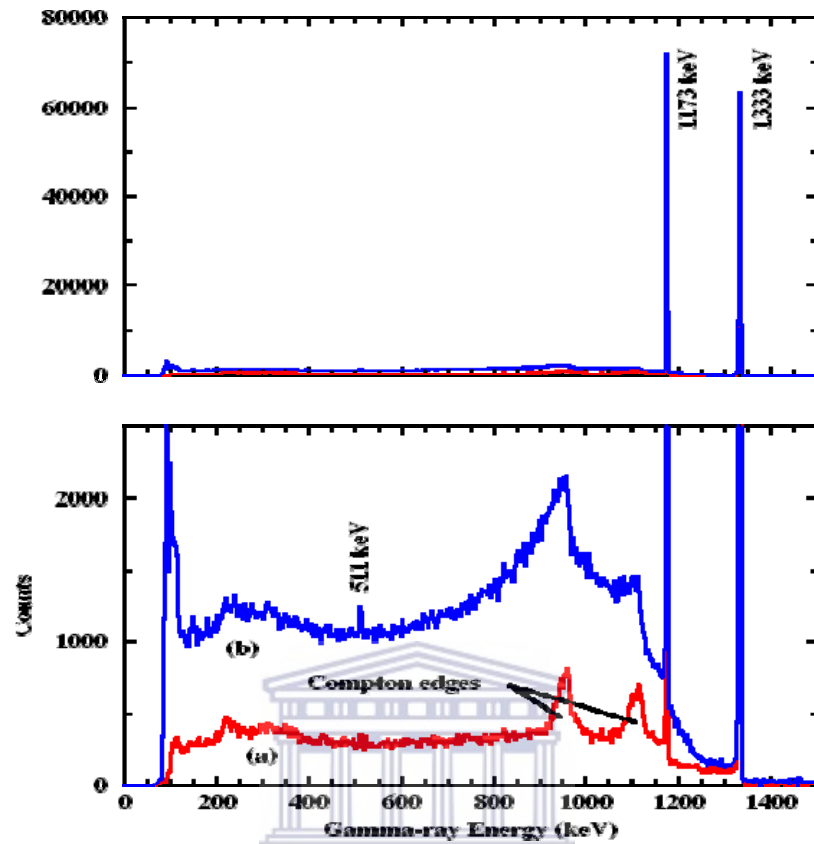
Figure 3-19: (a) suppressed and (b) unsuppressed spectra obtained with a ^{60}Co source. The upper panel shows the spectrum in full scale, emphasising the height of the two photo peaks relative to the Compton background. The second is expanded to show the reduction in the background due to escape suppression. The Compton edges and annihilation peak at 511 keV are labeled [Keė00].

All the 16 PM tubes for a given shield are then connected in series. The BGO signal from a Compton – scattered event vetoes the associated clover signal.

3.3.4 The AFRODITE spectrometer array

The AFRODITE (African Omnipurpose Detector for Innovative Techniques and Experiments) [New98] is a medium sized array that has the unique capability of detecting both high and low energy photons with a reasonably high efficiency by combining large volume escape suppressed HPGe detectors (clovers) with Low Energy Photon Spectrometer (LEPS) detectors [Mab03]. The AFRODITE comprises

of 8 clover detectors similar to those of EUROBALL III and 8 LEPS for photons with energies between 30 and 300 keV. It has an aluminum frame with a rhombicuboctahedron shape. The clover detectors are each housed in a Compton suppression shield that is made of bismuth germanate (BGO), which is a highly efficient scintillator for the detection of γ - rays [Em186, Lie84].
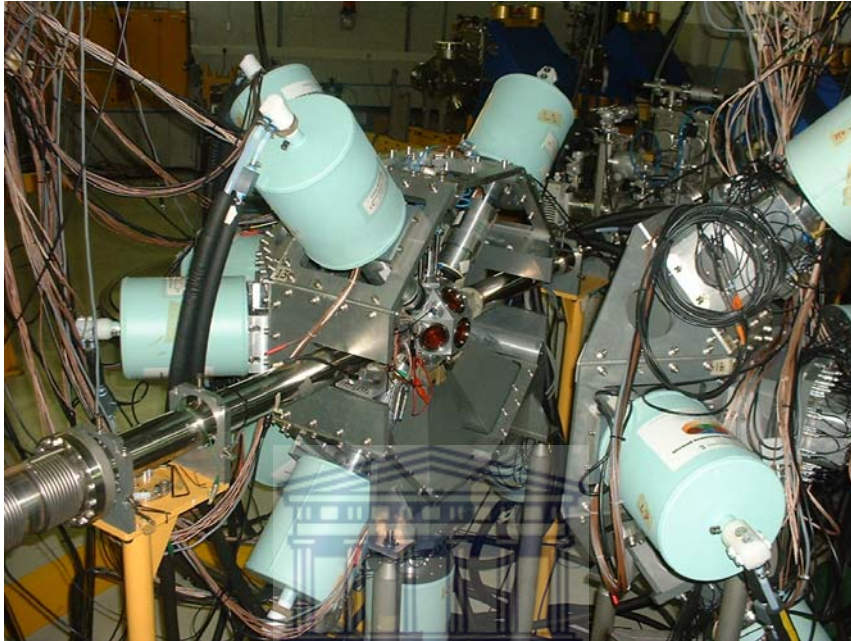
Figure 3-20: AFRODITE array with part of the support frame retracted, exposing the target chamber. The liquid nitrogen pipes to the detectors dewars have black insulation around them.

The AFRODITE is the γ - ray spectrometer built at iThemba LABS. It has 16 detectors positions relative to the beam, i.e. 16 square facets at 45°, 90° and 135° degrees. The AFRODITE array uses NIM Electronic and CAMAC clover modules, ADC's and TDC's. The AFRODITE array is shown in the Figure 3.20 with 8 clovers and 7 LEPS detectors. The target chamber is situated at the center of the array. The black pipes are supplying the liquid nitrogen to the dewars from a tank.

3.3.5 Frame, target chamber and target ladder

The aluminum frame supporting the 15 germanium detectors may be retracted from the beam line to allow access to the target chamber, as shown in Figure 3.21. The

target chamber was designed to afford a direct view of the target ladder through 25-micron kapton windows, which are flexible, transparent to γ - rays and maintain good vacuum. Inside the target chamber there is a target – ladder with a hydraulic positioner.
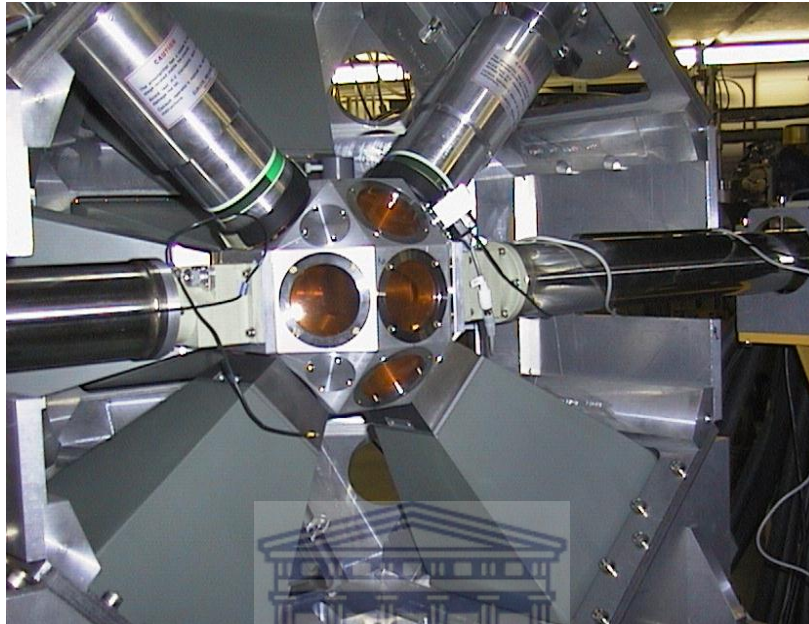
Figure 3-21: AFRODITE array and the target chamber with its kapton windows. A camera is mounted on the top right – hand triangular facet.

The target ladder usually supports aluminium oxide beam position monitor (top position), the target foil (bottom position), while the middle position is used for empty frame for checking the beam halo. A tantalum (which is 99.988 % ^{181}Ta and only 0.012 % ^{180}Ta) target with thickness of ≈ 1.0 mg/cm^2 (two foils of 0.5 mg/cm^2 each) was used for this experiment. The thin target was employed in order to prevent Doppler broadening of the peaks.

3.3.6   The electronics and data acquisition system

 Essentially all of the nuclear radiation detectors produce electronic pulses in response to the interaction with some ionizing radiation. These signals are processed by standardized nuclear instrumentation modules (Nuclear Instrumentation Module, NIM) to count the number of pulses or to more fully analyze the size or even the

shape of the signal. In addition, computer – based electronics in the CAMAC (Computer Automated Measurement and Control) system are used to measure the time relationships of pulses, the pulse heights, and the signal shape.

3.3.6.1   An overview of the kinds of modules used

The CAMAC and NIM Electronics fall into three broad categories: (i) *linear electronics* that maintain a linear relationship to the size of the initial signal, (ii) *logic circuits* that provide only a standard (or single sized) pulse indicating that a given logical condition was met, and (iii) *data – acquisition* for recording the data [Gil95].
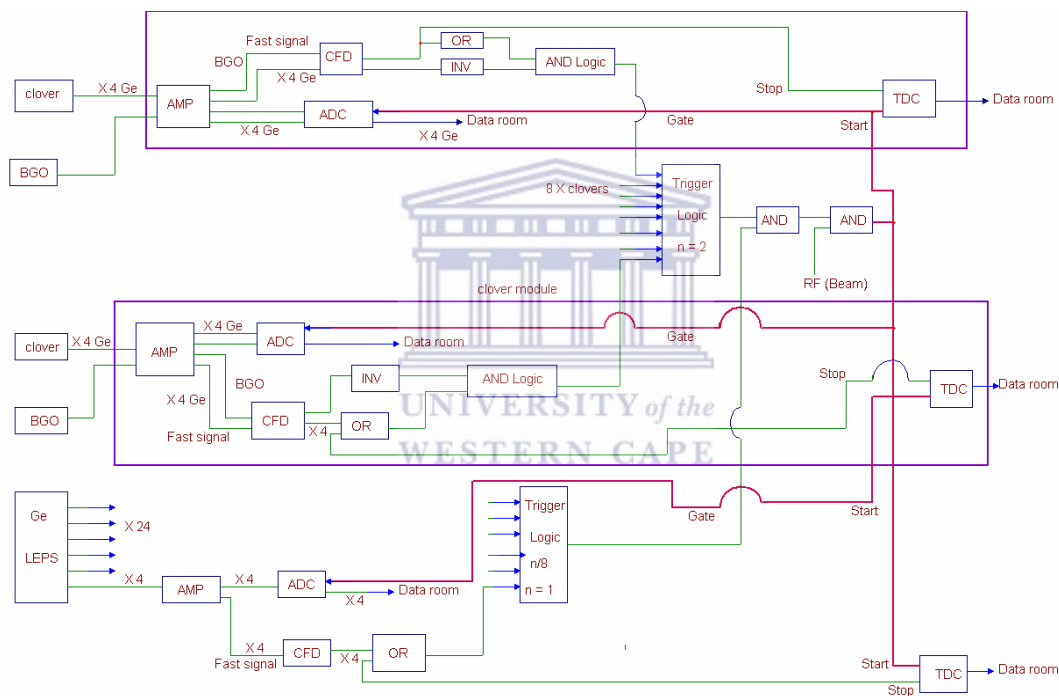
Figure 3-22: The AFRODITE array electronics setup for the experiment.

The NIM and CAMAC electronic units were connected according to the circuit diagram depicted in Figure 3.22. Standard NIM and CAMAC modules located in the experimental vault perform signal processing. Data acquisition used for this experiment was based on the MIDAS software package and the whole data acquisition system is directed from the data room. The MIDAS software was employed before (for energy calibration) and during the experiment. It was also used to monitor on – line spectra, event rate and data acquisition in general. Some of the

37

adjustable parameters (e.g. amplifier gains, shaping times and pole zero settings for the LEPS) can be set from the data room although trouble – shooting the electronics is only possible from within the vault itself. To explain the electronics used in this experiments let's look at the simple electronic circuit as shown in Figure 3.22.

Table 3.3: Electronic modules used in an AFRODITE array

Module	Model
Analogue-to Digital-Converter (ADC)	Silena 4418/V
Clover Module	RIS
Coincidence Unit	iThemba LABS
Constant Fraction Discriminator (CFD)	CAEN N415 or Ortec 934
Discriminator	Phillips 711 or LeCroy 821
Dual Gate Generator (DGG)	LeCroy 222
Event Trigger	iThemba LABS
Logic Fan-In/Fan-Out (FIFO)	LeCroy 429
NIM-ECL converter	EDA54 (iThemba LABS)
Quad Four-Fold Logic Unit (QFFLU)	Phillips 755
Spectroscopy Amplifier	CAEN N568
Stretcher	iThemba LABS
Time Amplitude Converter (TAC)	Silena 4418/T
Timing Filter Amplifier (TFA)	Ortec 474

The electronic diagram depicted in Figure 3.22 consists of two sub – circuits, namely, (i) a timing circuit, which is used to time – correlate the detected γ - rays and (ii) an energy circuit, which gives us information about the energy of the detected γ - rays. This energy information will then be used in the construction of γ - γ matrix.

3.3.6.2   Energy circuit

In most cases the detected energy is related to the total charge produced in the detector. For the best achievable energy resolution an optimum filter has to be implemented which takes into account the response as well as the noise characteristics

of the instrument. The essential element for signal processing chain is the pre –
amplifier housed in the detector cryostat and is usually located as close as possible to
the detector in order to minimize the noise signal [Gil95]. In earlier detector systems,
cables were used to connect the detector to the pre – amplifier, but presently the pre –
amplifier comes as an integral part of the detector assembly. This implies that the pre
– amplifier is cooled down whenever the detector system is being cooled, which also
reduces the electronic noise. The pre – amplifier in general can have various modes of
operation: current – sensitive, voltage – sensitive and charge – sensitive. The main
purpose of the pre – amplifier is to match the impendence of the detector (which is a
measure of the opposition to the flow of an alternating current). The charges are
created within the detector by the interaction with the gamma – radiation (as discussed
in section 3.2) and are then collected by the pre – amplifier, which converts the charge
pulse to a voltage pulse and drives the pulse to the next element in the circuit, which
is the spectroscopy amplifier [Leo87].

The pre – amplifier output pulse is ≈ 100 mV with a decay time of 50 μsec and is fed
to the spectroscopy amplifier. The amplifier gives two outputs, which are the fast and
the slow output. The fast output is used for the timing circuit and the slow (energy
signal) output is used for the energy circuit. For the slow signal the essential function
of the amplifier is to amplify the signal from the pre – amplifier and shape it into a
Gaussian pulse, so that the pulse height can be measured. It does this by electronically
differentiating and integrating the input signal and gives an output linear pulse, whose
height is proportional to the γ - energy. The other setting of the amplifier, called the
pole zero cancellation differentiation, removes the overshooting and undershooting of
the signal and allows the system to work under moderate count rate without loss of
resolution. (This was done in the vault during the experiment setup). The slow energy
signal is fed to the ADC (Analog – to – Digital Converter). The ADC is a device,
which converts the information contained in an analogy signal to an equivalent digital
form and this digitized signal is sent to the data room.

3.3.6.3 Timing circuit

To determine the time of the incoming particle (e.g. the start of the signal) FIR (Finite
impulse response) filters or procedures are used in analog circuit, such as the constant

– fraction method. The timing circuit establishes all the coincidence relationships between signals from different hardware components for a specific experiment. Here a signal from the BGO was used to veto the corresponding clover signal and coincidence was set between at least two "clean Ge" signals.

The pre – amplifier produces a negative shape pulse that goes to an amplifier (CAEN), which gives out a narrow negative signal. The output signals (from BGO and Ge) are fed to the CFD (Constant Fraction Discriminator) where they are converted to logic signals, which is required by the timing circuit. The BGO logic signal from CFD is inverted and fed to AND logic module to check the coincidence between the BGO and clover. The condition for coincidence is met when both input signals are present in the AND logic. If any one of the signals is not present the AND logic module will give zero output. Thus the AND module is going to give an output logic signal provided the BGO is not hit by a gamma ray. The four clover element logic signals are sent to an OR module, which gives an output provided at least one signal is present. The output signal is then fed to the trigger logic, where the module will determine whether there is a coincidence between the clovers. The trigger logic gives an output if there is a coincidence between at least $n_1 = 2$ clover signals. This logic signal is sent to another AND logic to check whether there is also a coincidence with at least $n_2 = 1$ LEPS detectors. Finally the signal is connected to another AND logic module for checking the coincidence with the beam RF logic signal. The output signal is fed to the ADC (as ADC gate signal) and to the TDC (as common start signal) modules. The TDC (time to digital converter) in the CAMAC crate has two inputs, which are common start and stop. Here the TDC produces digitalized output corresponding to the time between the start and stop signals. The TDC stop signal is provided by the first fast detector signal to arrive at the TDC after the TDC start pulse. Individual detectors generate the stop pulses. The digitized TDC output signal is sent to the data room.

CHAPTER 4

EXPERIMENTAL AND DATA ANALYSIS

The data presented in this work were taken in independent fusion – evaporation experiments, using the AFRODITE array to measure γ - γ coincidences. The heavy ion beam was provided by the K = 200 separated sector cyclotron facility of iThemba LABS. The present chapter details the experiment and methods used in the data analysis. The initial data analysis consisted of the following: energy calibration, gaindrift corrections and Doppler – shift corrections. After that the data were sorted into a γ – γ coincidence matrix, utilized to study the high – spin states of the ^{194}Tl nucleus.

4.1   Experimental procedure

The ^{18}O beam with a current of 20 nA delivered by the Separated Sector Cyclotron was utilized to populate high spin states in ^{194}Tl by means of the ^{181}Ta (^{18}O, 5n) ^{194}Tl reaction.
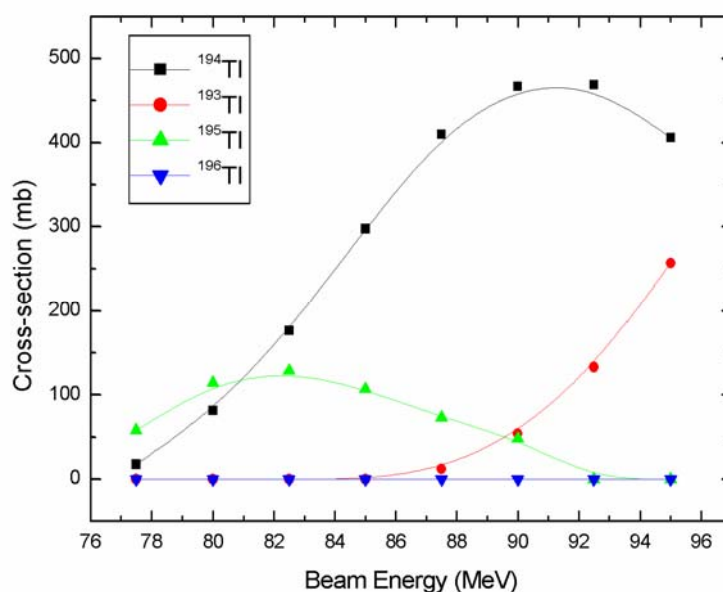
Figure 4-1: The excitation functions (cross – section σ) predicted by the statistical – model code PACE4 [Gav80, Gav 93] following the ^{18}O + ^{181}Ta reaction. The suitable beam energy of 93 MeV was chosen for this experiment.

The nuclei studied in this work were produced via heavy – ion fusion – evaporation reactions. In such reaction, the target and projectile nuclei fuse together, forming a compound nucleus. This idea of compound formation was first suggested by Neils Bohr in 1936 [Bohr 36]. The excitation functions for this reaction are presented in Figure 4.1, as predicted by the PACE4 statistical – model calculations [Gav80, Gav93]. These predictions were used to select the suitable beam energy for this reaction. The initially proposed reaction was $^{197}Au + {}^{4}He \rightarrow {}^{194}Tl + 7n$ at beam energy of 85 MeV. However it appeared that α beam with energies between 69 and 110 MeV is not possible to produce with the Separated Sector Cyclotron. Thus we chose the $^{181}Ta + {}^{18}O \rightarrow {}^{194}Tl + 5n$ reaction at 93 MeV. At the proposed beam energy the cross section for this reaction is 470 mb according to PACE 4 calculations.

Table 4.1: Summary of the experimental details.

45^{0} detectors	3 LEPS
90^{0} detectors	4 Clovers, 3 LEPS
135^{0} detectors	4 Clovers
Target	^{181}Ta
Beam	^{18}O
Beam – burst separation	69 ns
Beam energy	93 MeV
Pulse selection	no
Beam current	20 nA
Recoil velocity of the compound system, v/c %	0.80
Compound system	^{199}Tl
Dominant Residuals at 93 MeV (PACE4)	^{194}Tl (79.9 %) ^{195}Tl (6.45 %), ^{193}Tl (9.21 %), ^{194}Hg (2.62 %), ^{195}Hg (0.54 %), ^{192}Au (0.44 %), ^{191}Au (0.84 %)
Event Trigger Condition	$N \geq 2$
Count Rate	5.6 kHz
Readout	CAMAC
Beam Time	48 hrs

Thin metallic tantalum (99.988 % ^{181}Ta) foils with thickness of 0.5 mg/cm^2 per foil were used. We have used a stack of two foils with total thickness of 1.0 mg/cm^2. Such thin target was employed in order to avoid Doppler broadening of the peaks. Gamma – ray spectroscopy was performed with the AFRODITE Ge array (described in chapter 3). One weekend of beam time was approved for this experiment. Since we lost about 18 hours beam time due to problems with the RF (Radio frequency) system and since there was a spare weekend without suitable users for the beam, a second weekend of beam time was allocated to this experiment. The data analyzed in this work was obtained in the second weekend. The trigger logic was set to accept events when at least two clover detectors fired in coincidence. The counting rate was about 5.6 kHz.

4.2   Data acquisition

The data acquisition system used for this experiment was based on the MIDAS software package. During the experiment on – line spectra, event rates and data acquisition in general were monitored. Events containing both timing and energy information were written on the digital linear tapes (DLT). Every two hours the on – line spectra were saved on the hard disc.

4.3   Energy calibrations

The energy calibration was done before running the experiment using the ^{152}Eu and ^{133}Ba radioactive sources. The ^{152}Eu source emits gamma – rays in the energy range 45 – 1408 keV and the ^{133}Ba source in the energy range 30 – 400 keV (which include the X – rays for these elements). The first run was done with the ^{152}Eu source and took 29 minutes. The source was placed in the center of the chamber. The centroids of the photopeaks from the ^{152}Eu and ^{133}Ba spectra were found using a peak – fitting program. The absorbers used on the clovers were of Cu with thickness of ~ 0.27 mm and for the LEPS were Al with thickness of ~ 0.6 mm. The energy calibration after running the experiment was done by using the same spectra.

4.4   Gaindrift corrections

This analysis was aimed at tracking possible detector (LEPS and Clovers) gain drifts that might have occurred during the experiment. Gaindrifts of 1 – 3 keV were observed between some of the runs. According to investigations done by D. Dowie and S.M. Mullins the gain drifts are likely related to that temperature fluctuation in the AFRODITE vault, which may affect the amplifiers and lead to a drift of the output signals [Dow00]. Therefore, it was necessary to perform gaindrift corrections as part of the data analysis procedure. In order to perform these corrections there must be reference spectra (RS) in most cases obtained from the first runs for the LEPS and clover elements (already gain matched and calibrated). The peak – shifts which are the channel differences between the reference peaks (of the RS) and the shifted peaks are determined from $(P_{1l}) - (P_{2l}) = S_l$ and $(P_{1h}) - (P_{2h}) = S_h$, where S_l and S_h are the peak – shifts in channels for one peak at the low and one peak at high energy respectively and P_{1l}, P_{1h} and P_{2h}, P_{2h} are the positions in channels of the peaks at low and high energies and P_{2h} and P_{2h} are the positions of the peaks in the reference spectrum.

The final parameters a' and b' for the clovers were calculated using the equations below 4.1 and 4.2:

$$a' = \frac{a(P_{2h} - P_{2l})}{(P_{2h} + S_h) - (P_{2l} + S_l)}$$ (4.1)

$$b' = \frac{(P_{2l}S_h - P_{2h}S_l)}{(P_{2h} + S_h - P_{2l} - S_l)} + b\frac{(P_{2h} - P_{2l})}{(P_{2h} + S_h - P_{2l} - S_l)}$$ (4.2)

where the final parameter a' is the slope or gain and b is the old offset and b' the new offset.

The data were then sorted using the new calculated parameter a' and b' and hence the peaks were observed in the same channel number in all runs. This maintained a good energy resolution.

44

4.5 Doppler – shift corrections

Doppler shift corrections for the detected γ – rays were necessitated since a thin [181]Ta target was used for this experiment. The residual nuclei recoil into vacuum so that the detected γ – rays were subjected to energy shift according to the equation:

$$E_\gamma = E_0 \left(1 + \beta \cos \theta \right) \qquad (4.3)$$

where

(i) E_γ is the Doppler shifted γ – ray energy

(ii) E_0 is the unshifted γ – ray energy detected normal to the recoil nucleus velocity axis

(iii) θ is the angle at which the γ – ray is detected with respect to the beam direction

(iv) $\beta = \frac{v}{c}$, where v is the recoil velocity of the nucleus and c is the speed of light.

The Doppler shift for the γ – rays emitted by the recoiling [194]Tl nuclei have been measured for the clover elements located at 85^0, 95^0, 130^0 and 140^0.
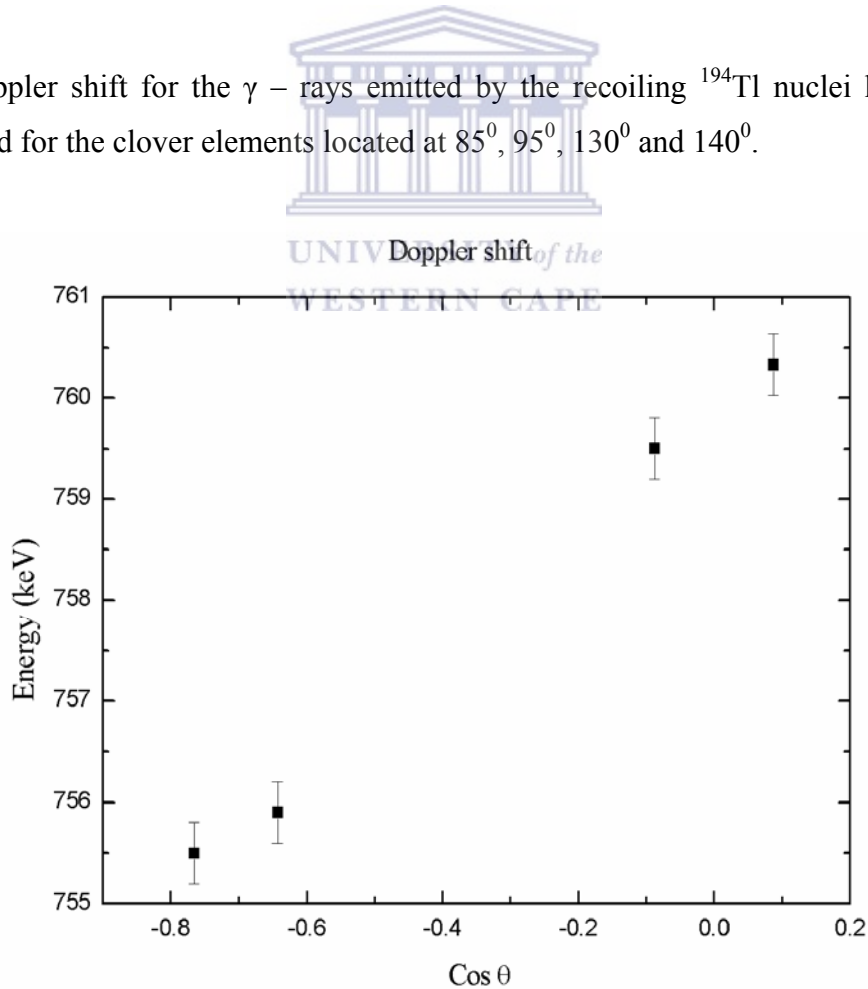
Figure 4-2: Shows the Doppler shift of the peak on the 760 keV peak.

Doppler shifts were measured for the peaks with energies of 523.3 keV, 687.3 keV, 760.3 keV, 781.1 keV and 1059.3 keV and two examples of the measured energy (keV) versus cos θ are shown in Figures 4.2 and 4.3. The equation 4.3 was used to calculate the recoil velocities for these peaks and the average value obtained was $\beta \approx$ 0.80 ± 0.04 %.
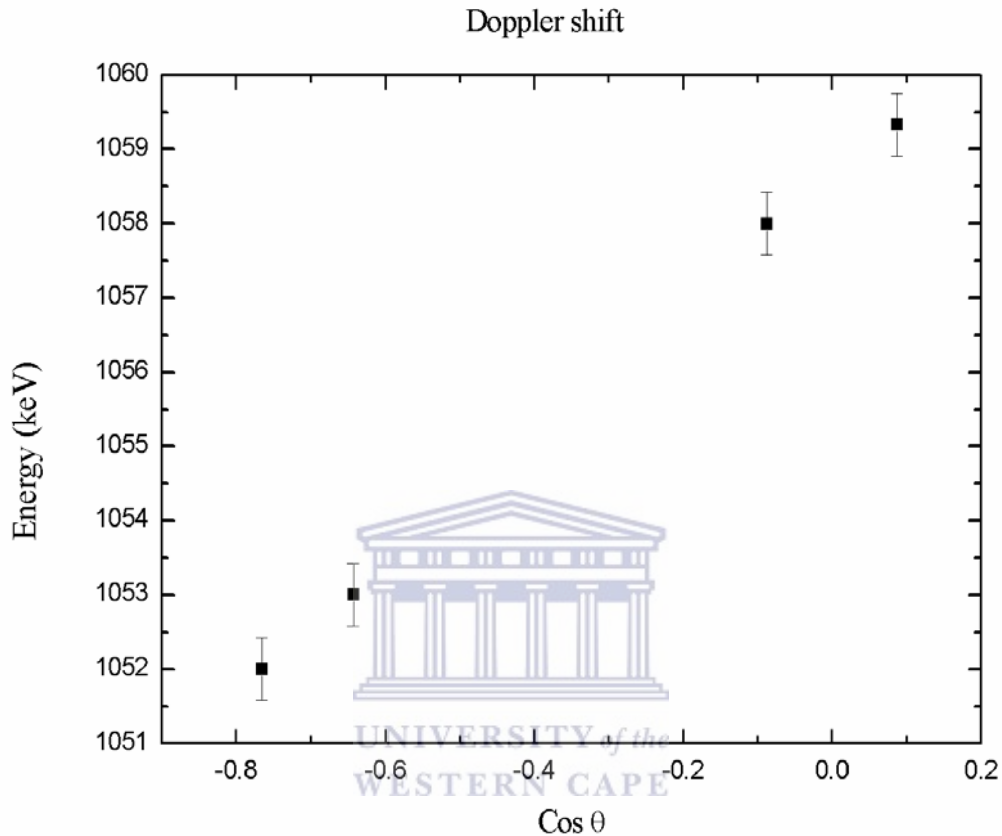
Figure 4-3: Shows the Doppler shift of the peak on the 1059 keV.

4.6   Constructing a γ - γ coincidence matrix

In our experiment a γ- γ coincidence occurs if two γ - rays ($E_{\gamma 1}$ and $E_{\gamma 2}$) are detected during a resolving time (200 ns). A 3 - dimensional symmetric matrix was constructed by using γ - γ coincidences, with E_γ on the x and y-axes and coincidence counts on the z-axis. An event constitutes all γ- rays that are detected in coincidence. Let us consider a coincidence event of three γ - rays, e.g. $E_{\gamma 1}$, $E_{\gamma 2}$ and $E_{\gamma 3}$. All possible coincidence pairs are then formed e.g. ($E_{\gamma 1}$, $E_{\gamma 2}$), ($E_{\gamma 2}$, $E_{\gamma 1}$), ($E_{\gamma 1}$, $E_{\gamma 3}$), ($E_{\gamma 3}$, $E_{\gamma 1}$), ($E_{\gamma 2}$, $E_{\gamma 3}$) and ($E_{\gamma 3}$, $E_{\gamma 2}$). The coincidence pairs are represented in a matrix, by coordinates

(x, y, z). For instance the pair $(E_{\gamma 1}, E_{\gamma 2})$ corresponds to coordinates $(E_{\gamma 1}, E_{\gamma 2}, Z_1)$, and the pair $(E_{\gamma 2}, E_{\gamma 1})$ corresponds to coordinates $(E_{\gamma 2}, E_{\gamma 1}, Z_2)$. The coordinate Z_1 is the counts on the z-axis and it represents the number of instances the pair $(E_{\gamma 1}, E_{\gamma 2})$ is found in the data. Similarly Z_2 represents the number of instances the pair $(E_{\gamma 2}, E_{\gamma 1})$ is detected in the data and therefore $Z_1 = Z_2$, and the matrix is symmetric. For every instance a coincidence pair e.g. $(E_{\gamma 1}, E_{\gamma 2})$ is detected, the coincidence counts coordinate Z_1 is incremented. In general a matrix is constructed by incrementing the corresponding coincidence counts Z for a specific pair each time this pair is found in the data.

4.7 Gating

Gating is the same as slicing a region around γ - ray's energy E_γ on the x (or y) axis in the matrix. Let us consider for instance the level scheme in Figure 4.4.
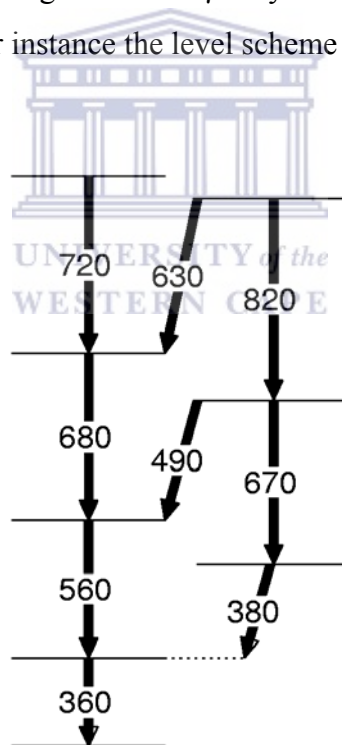
Figure 4-4: Part of a level scheme

It can be seen that: (i) 360 keV transition is in coincidence with all the other γ - rays, (ii) 560 keV transition is in coincidence with 720 keV, 680 keV, 360 keV, 820 keV, 670 keV, 630 keV and 490 keV transitions, but is not in coincidence with 670 keV

and 380 keV γ - rays. (iii) 380 keV transition is in coincidence with 360 keV, 670 keV and 820 keV, but is not in coincidence with 720 keV, 680 keV, 630 keV, 680 keV, 490 keV and 560 keV. In this work the coincidence relationships of the γ -transitions are studied and used to extend the level scheme of ^{194}Tl. By minimizing the width of the time gate, the number of random coincidences can be kept at an acceptable level. However if the nuclear level is metastable, or isomeric, it is possible that all transitions that are below (or after) this level will end up outside this time gate if the gate is started by a transition above this level. In such a case, the levels below and above the isomeric state can be tied together by increasing the time gate. In general a level scheme for a certain nucleus can be constructed by analyzing gated spectra with gate set on different γ - ray energies and by considering intensities analysis.

4.8   Construction of the level schemes

The construction of the level scheme involves studying the coincidence relationships between the detected γ - rays from the background subtracted gated spectra (with the aid of the ESCL8R [Rad95] software program). A gate can be set on a particular photopeak using channel numbers determined from the total projection of other spectrum to produce a coincidence spectrum of all the γ - rays in coincidence with that transition. Following this procedure, several known transitions associated with ^{194}Tl [Kre79] were observed. Apart from the fact that several new transitions were placed in the ^{194}Tl level scheme. γ - coincidence analysis had led to considerable extension of the level schemes of ^{194}Tl. The total projection spectrum extracted from an online matrix and associated to the reaction used is shown in Figure 4.5.
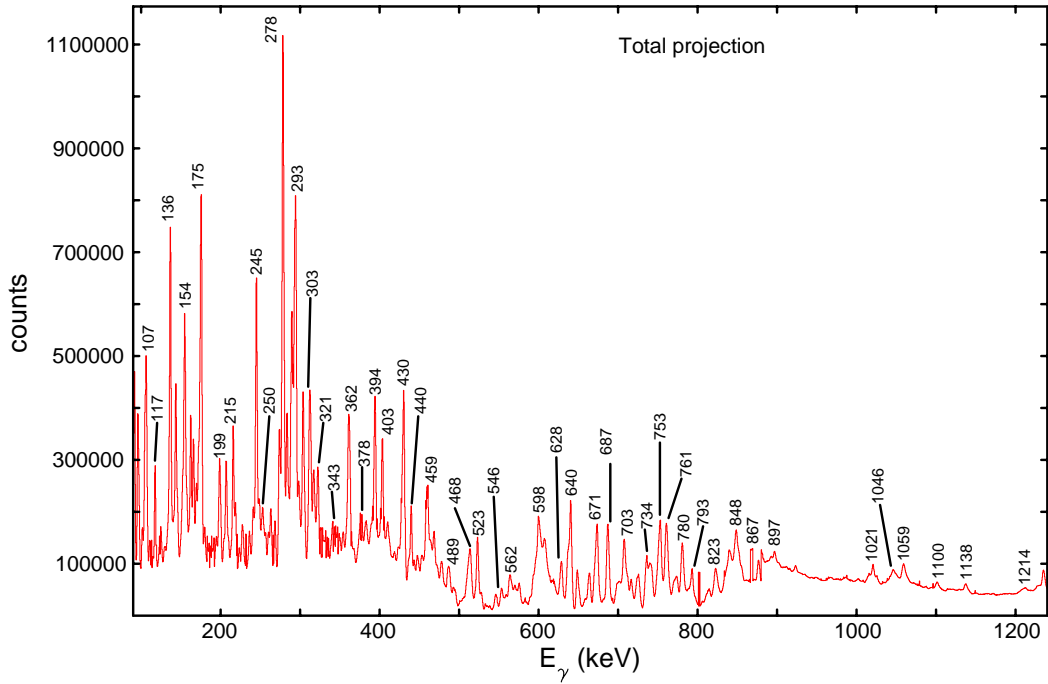
Figure 4-5: The total projection spectrum obtained from the online matrix with the known transitions, which are marked by stars.

4.9   DCO ratios

The Directional Correlations from Orientated states (DCO) method can be used to infer the spin differences between states observed by the measurement of the gamma – decay between them [Kra73, Krä89, Bar87]. It is similar to angular distribution measurements. The DCO ratios help us to differentiate between transitions of different multipolarities. It is often used with small arrays or when gamma rays with small intensities are measured. In the AFRODITE Ge array the detectors are arranged at different angles with respect to the beam direction. The clover detectors of the array are placed at 90^0 and 135^0. Thus the detector angles are usually fixed in such an experiment. The data of ^{194}Tl was sorted into two angle gated γ – γ coincidence matrices. These two-dimensional spectra correlate the intensities of the coincidence transitions in a single cascade and the angle at which the gamma – rays were measured. One matrix (called asymmetric) consisted of the coincidences between γ – rays detected at 135^0 (y – axis) and those detected at 90^0 (x – axis). The second one (symmetric) consisted of coincidences between 135^0 only. The same gates were made

on the y-axes in both symmetric and asymmetric matrices, to obtain 135^0 and 90^0 spectra respectively. The background spectra were made by setting gates on the background region close to the measured peak in both symmetric and asymmetric matrices. The 135^0 and 90^0 background spectra were subtracted from the 135^0 and 90^0 spectra respectively. Background subtraction reduces the amount of contamination from the neighboring thallium nuclei, and thereby intensifies the ^{194}Tl peaks in the final spectra.

The DCO ratios for the γ – rays of interest were determined as:

$$R_{DCO} = \frac{A(135^0)}{A(90^0)} \qquad (4.4)$$

where A (135^0) is the area of the peak in the 135^0 gated spectrum (with background subtraction) and A (90^0) in the 90^0 gated spectrum (with background subtraction) respectively. By taking the ratio of the number of counts for a given transition in these two spectra, a DCO ratio can be obtained, which can be used to distinguish between different multipolarities. The R_{DCO} for a number of known dipole and quadrupole transitions in ^{194}Tl [Kre79] were calculated from these background subtracted spectra. Average R_{DCO} values of 0.5 and 0.8 were obtained for the known stretched dipole (ΔI = 1) and stretched quadrupole (ΔI = 2) transitions respectively. With these measurements it was easier to assign the spin and (sometimes) parity to the new transitions.

CHAPTER 5

EXPERIMENTAL RESULTS OF DATA ANALYSIS

This chapter presents the experimental results of the γ - γ coincidence analysis and the DCO ratios measurements concerning the high – spin states studies of the ^{194}Tl nucleus, performed in this work.

5.1   Level scheme of ^{194}Tl

The known level scheme of ^{194}Tl established in a previous study [Kre79] consisting of a single band of 14 transitions and 11 levels, and is shown in Figure 5.1.
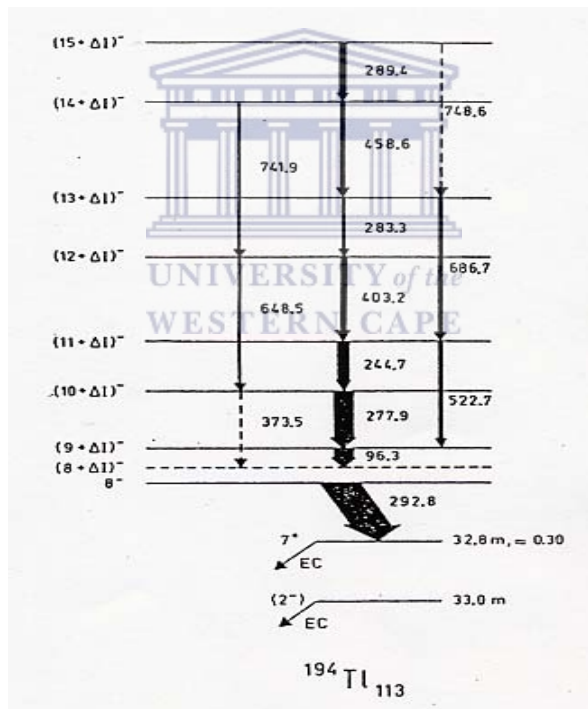
Figure 5-1: The known level scheme deduced from the previous studies of high – spin states [Kre79].

The confirmation of the previously suggested transitions was done before the level scheme in Figure 5.1 was extended to higher excitation energies. Our data are in agreement with most of the placements of the transitions in Figure 5.1. The level scheme determined in this work from the γ - γ coincidences analysis of the AFRODITE data, with bands labeled numerically, is presented in Figure 5.2.
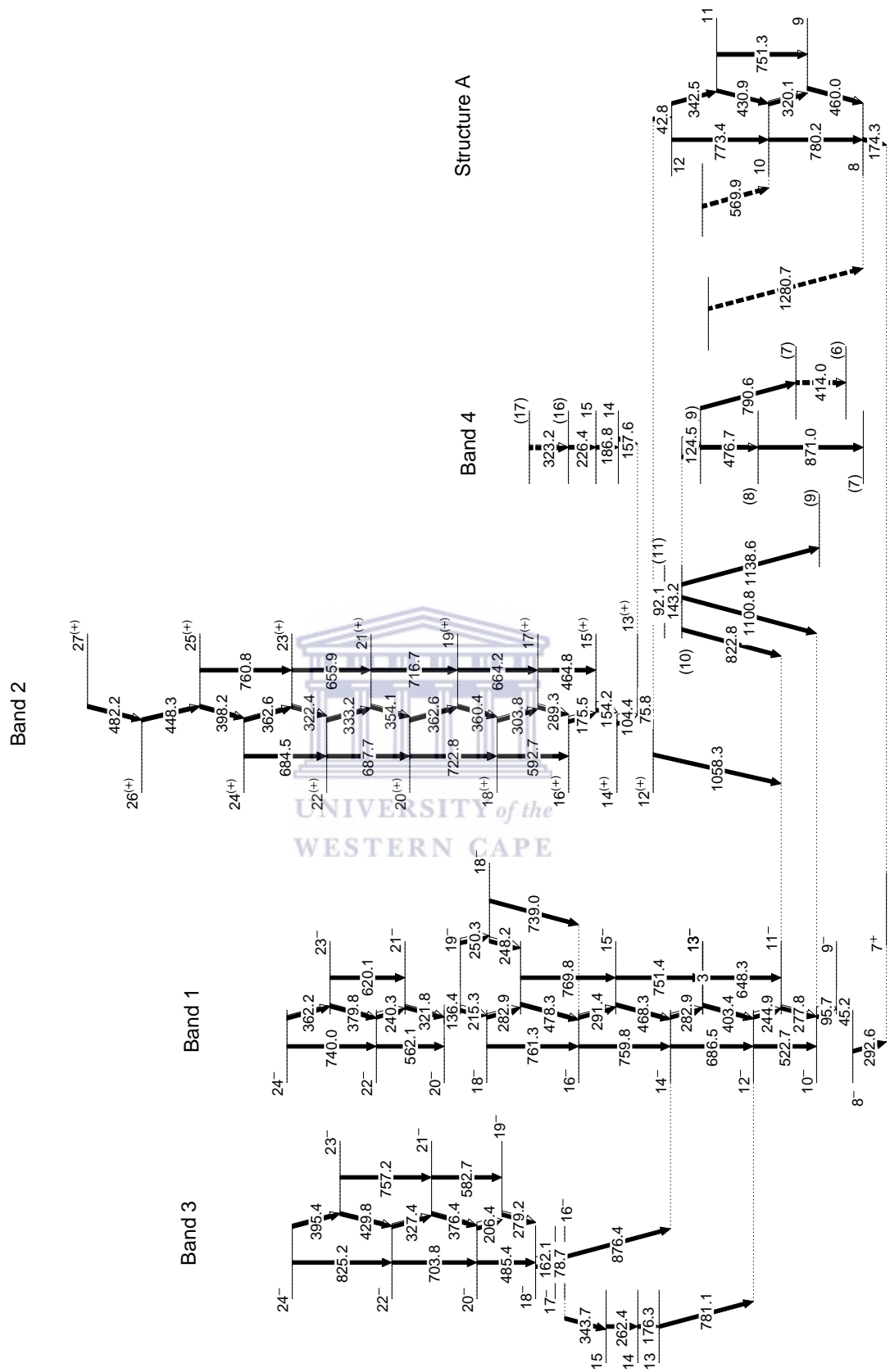
Figure 5-2: The proposed level scheme of ^{194}Tl based on the present work. The transition energies are given in keV. Tentative transitions are denoted with dashed lines and brackets

The present level scheme extends the work of [Kre79] et al. The band 1 was extended to higher spins and three new bands were observed in this work. About 88 new transitions have been placed in the level scheme. The placement of the transitions in the level scheme was based on the coincidence relations between these transitions and excitation energy sums and differences. The level scheme was extended up to spin of 27 ℏ and it is composed of 102 transitions and 69 energy levels. The DCO ratios measurements were performed in order to help us to assign spins and parities to the new levels. The results of this experiment are consistent and allows us to establish the spin (and in many case the parity) values of almost all of the identified levels in ^{194}Tl.

Band 1

Band 1 was extended to higher excitation energy and spin of 24⁻. Few changes have been made to the previously suggested level scheme. Mainly, the 289 keV transition have been placed in the new band 2 ($16^{(+)} \rightarrow 17^{(+)}$), the 741.9 keV ($22^- \rightarrow 24^-$) has been placed at higher excitation energy in the level scheme, and 458.6 keV transition was removed completely from band 1 and assigned to structure A. A new transition of 45 keV was observed between the 292.6 and 96.3 keV transitions and is shown in Figure 5.3
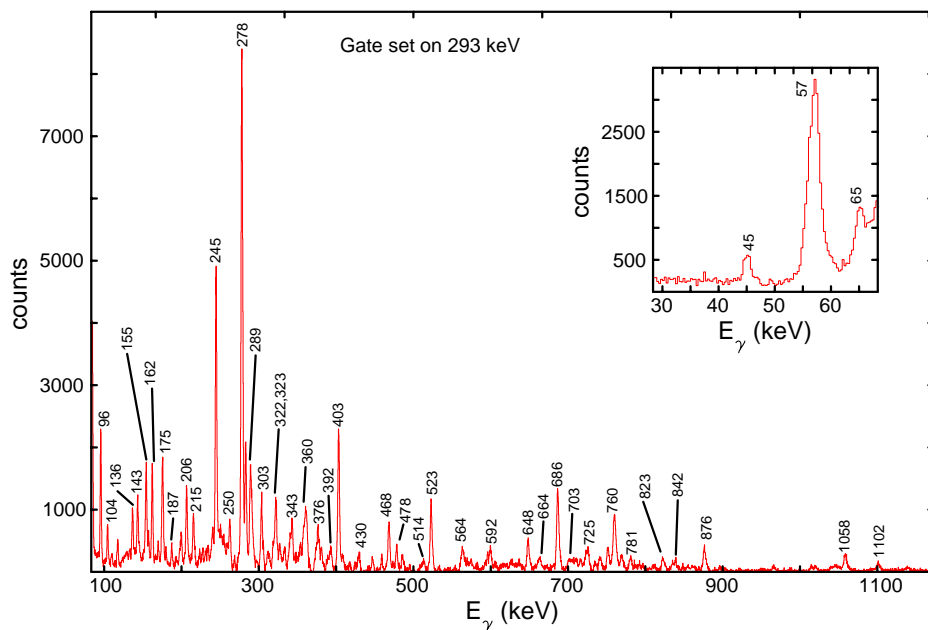
Figure 5-3: The γ - ray coincidence spectrum gated on the 293 keV transition. The insert shows the expansion of this spectrum at low energies

Finally the two tentative transitions (373 and 748.6 keV) were removed from the level scheme, because our data could not confirm their presence.
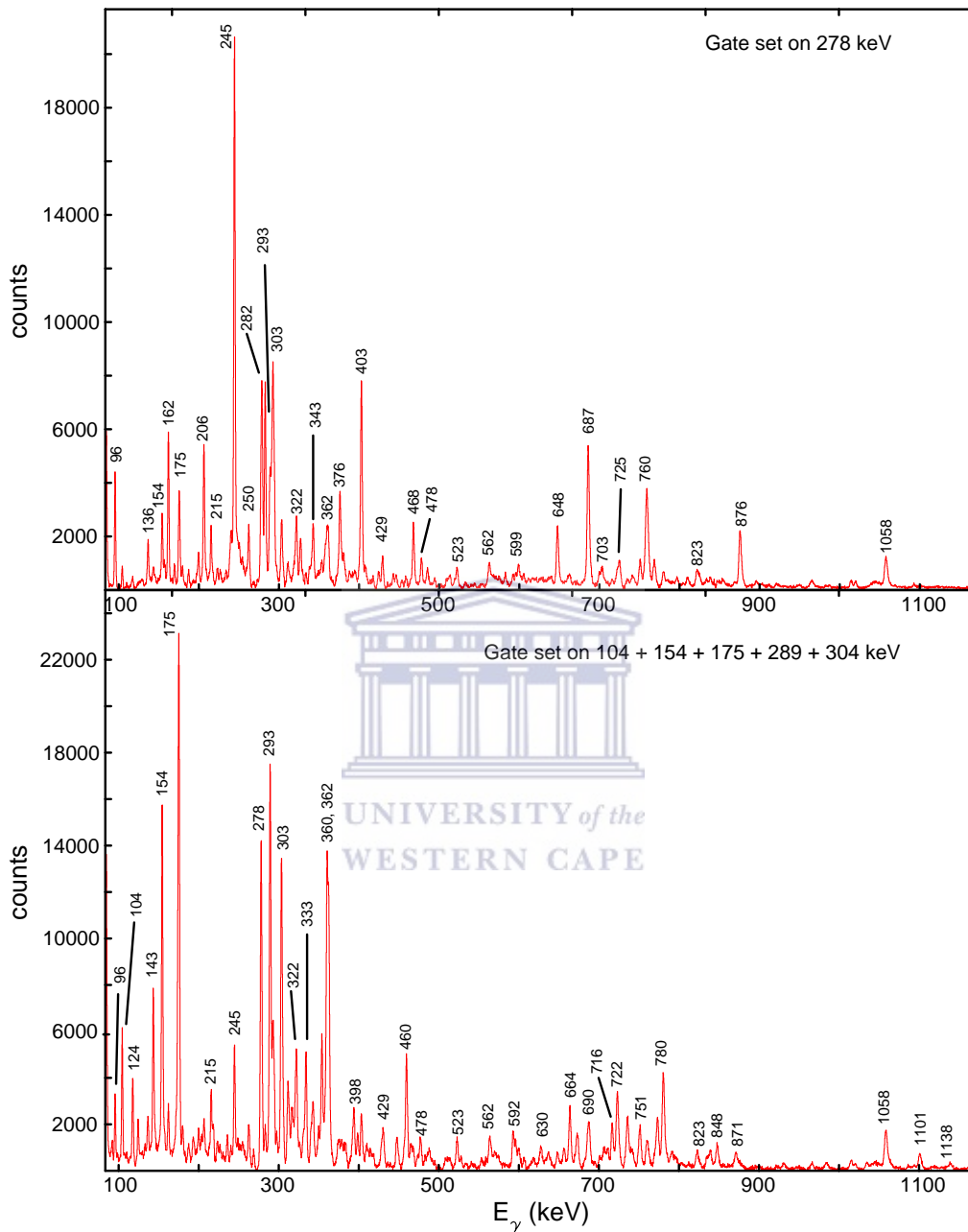
Figure 5-4: The γ - rays coincidence spectra gated on the (a) 278 keV and (b) the sum of (104 + 154 + 289 + 304) keV transitions. All the γ - rays seen in coincidence with the gate in both panels are labeled with their respective energies. The top panel shows most of the transitions in band 1 and the bottom panel shows the transitions in band 2.

All transitions between the levels with spins of 14⁻ to 24⁻ are new. The transitions of band 1 are shown in the top panel of Figure 5.4, where a spectrum gated on the 278

keV γ – ray is plotted. Band 1 also shows some doublet transitions such as 282.9 and 761.3 keV transitions which are shown in the Figure 5.5. Figure 5.5 shows two spectra one of them is gated on the 760 keV (top panel) transition and indicates that the 760 keV transition is a doublet because another γ - ray with energy of ~ 760 keV is observed. The second spectrum is gated on the 282 keV transition (bottom panel) and shows that the 282 keV transition is also a doublet. Figure 5.6 shows two gated spectra which confirm the presence of 761 and 760 keV transitions.
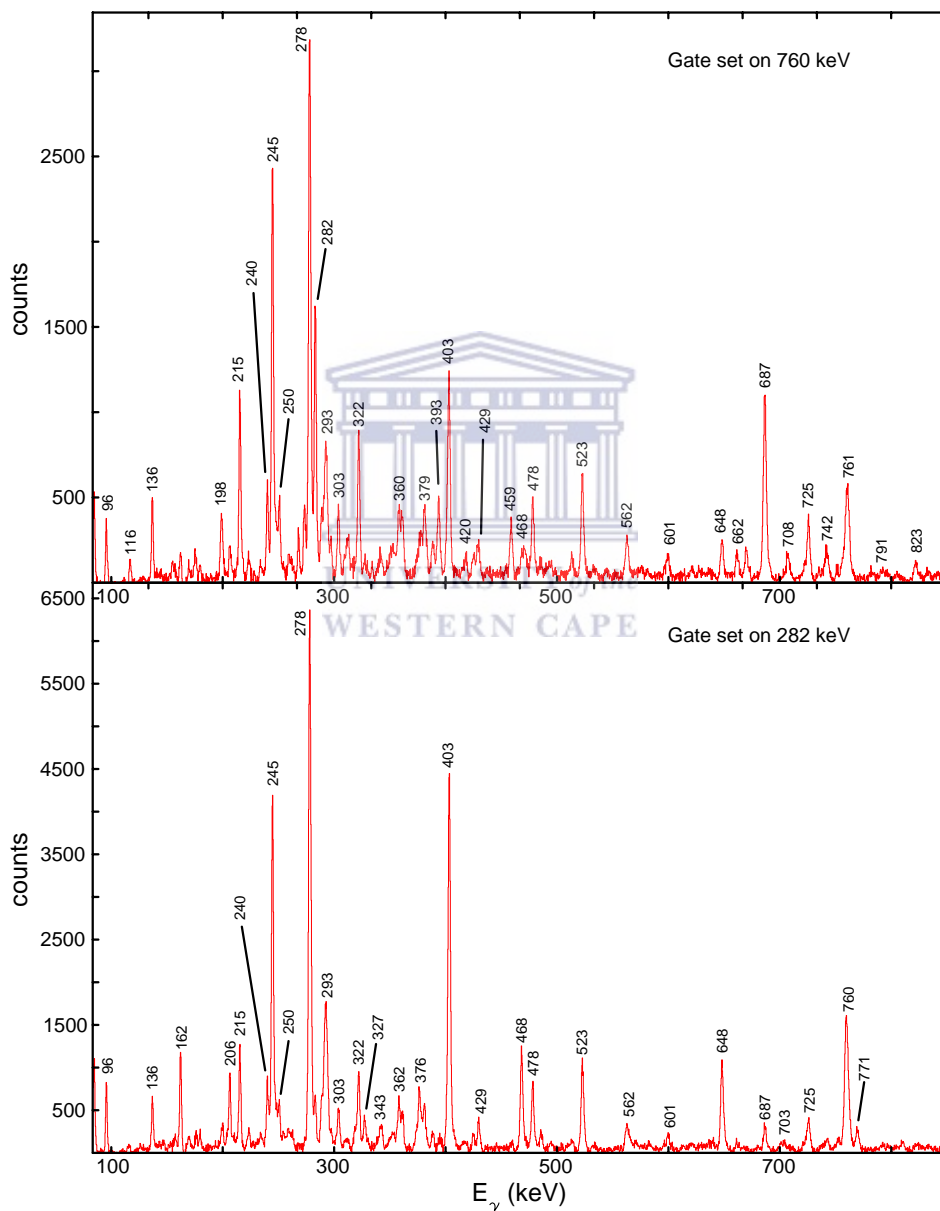
Figure 5-5: The γ – rays coincidence spectra gated on the (a) 760 (top panel) and 282 (bottom panel) keV transitions. They show the 760 keV and 282 keV transitions are selfcoincident, and therefore double.

The 761 and 760 keV transitions are seen clearly in the spectra gated on the 468 and 478 keV transitions respectively, because the 468 keV transition is in anticoincidence with the 760 keV transition and in coincidence with the 761 keV transition, while it is the opposite for the 478 keV transition.
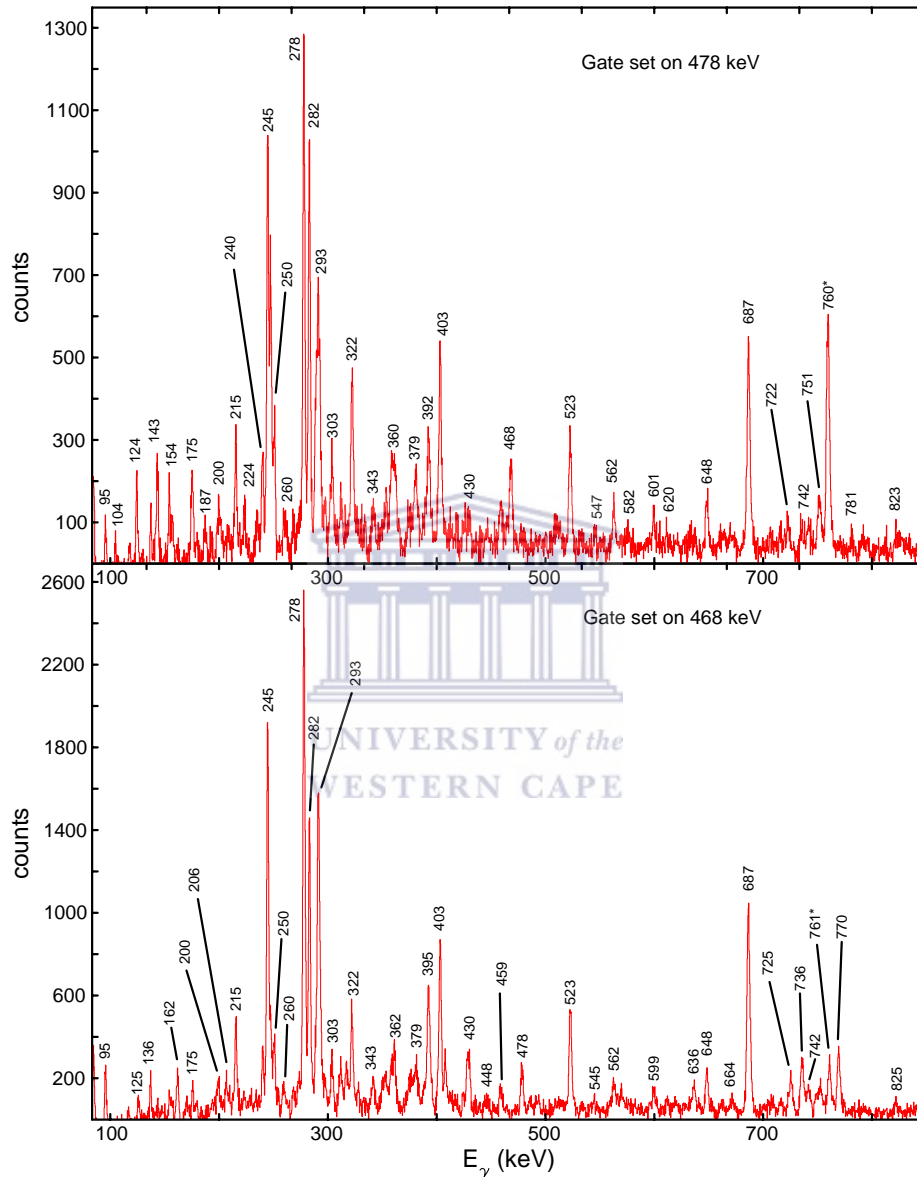
Figure 5-6: The γ – rays in coincidence with the (a) 478 keV transition (top panel) and (b) 468 keV transition (bottom panel).

Band 2

Band 2 is composed of new transitions only, except for the 289 keV transition, which was previously placed in band 1. Band 2 is based on the $I^\pi = 12^{(+)}$ state and consist of

a sequence of M1 and E2 transitions up to the $I^\pi = 27^{(+)}$ state. Tentative parity is assigned for band 2.
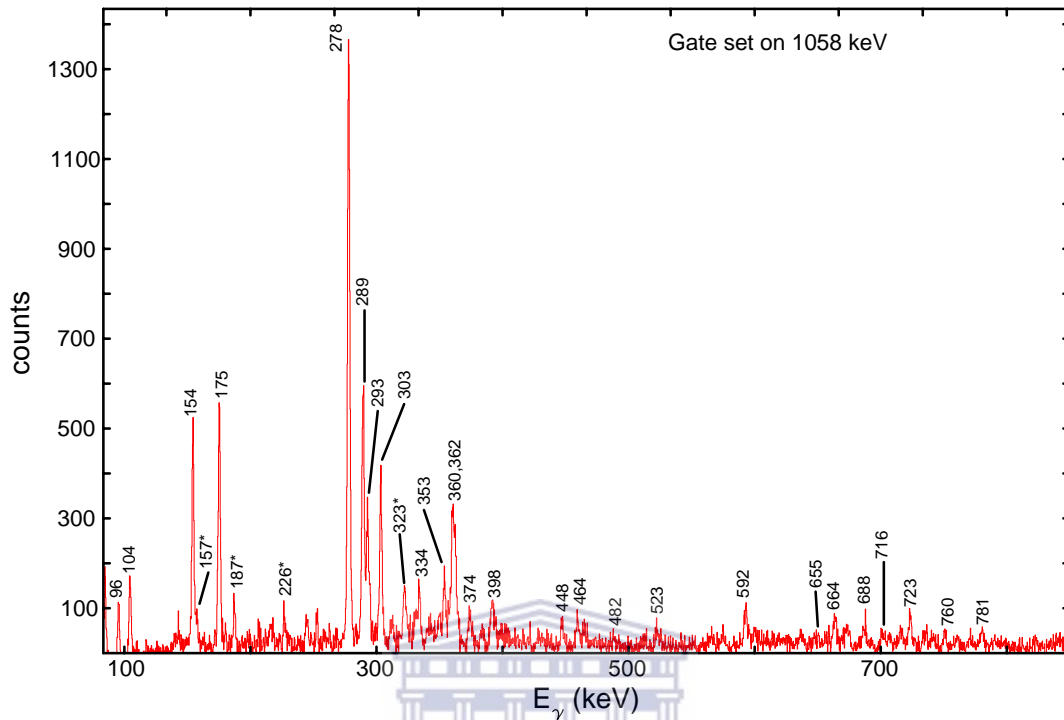
Figure 5-7: The γ - ray coincidence spectrum gated on the 1058 keV transition. All the γ - rays seen in coincidence are labeled with their respective energies.

A spectrum gated on the 1058 keV transition shows the transitions in band 2 and is shown in Figure 5.7. Band 2 transitions can also be seen in a spectrum gated on the sum of the 104, 154, 289 and 304 keV transitions as shown in Figure 5.4. Few doublet transitions were observed in band 2, such as two 362 keV and one 360 keV transitions shown in the spectra gated on the 687 and 362 keV transitions in Figure 5.8.

Band 3

The band 3 is composed of 13 transitions and decays to the $I^\pi = 12^-$ and $I^\pi = 14^-$ levels of band 1. It is new and extends up to the $I^\pi = 24^-$ level. The band is composed of M1 and E2 transitions. Figure 5.9 shows the transitions of band 3 in a spectrum gated on the 162 keV transition.

57
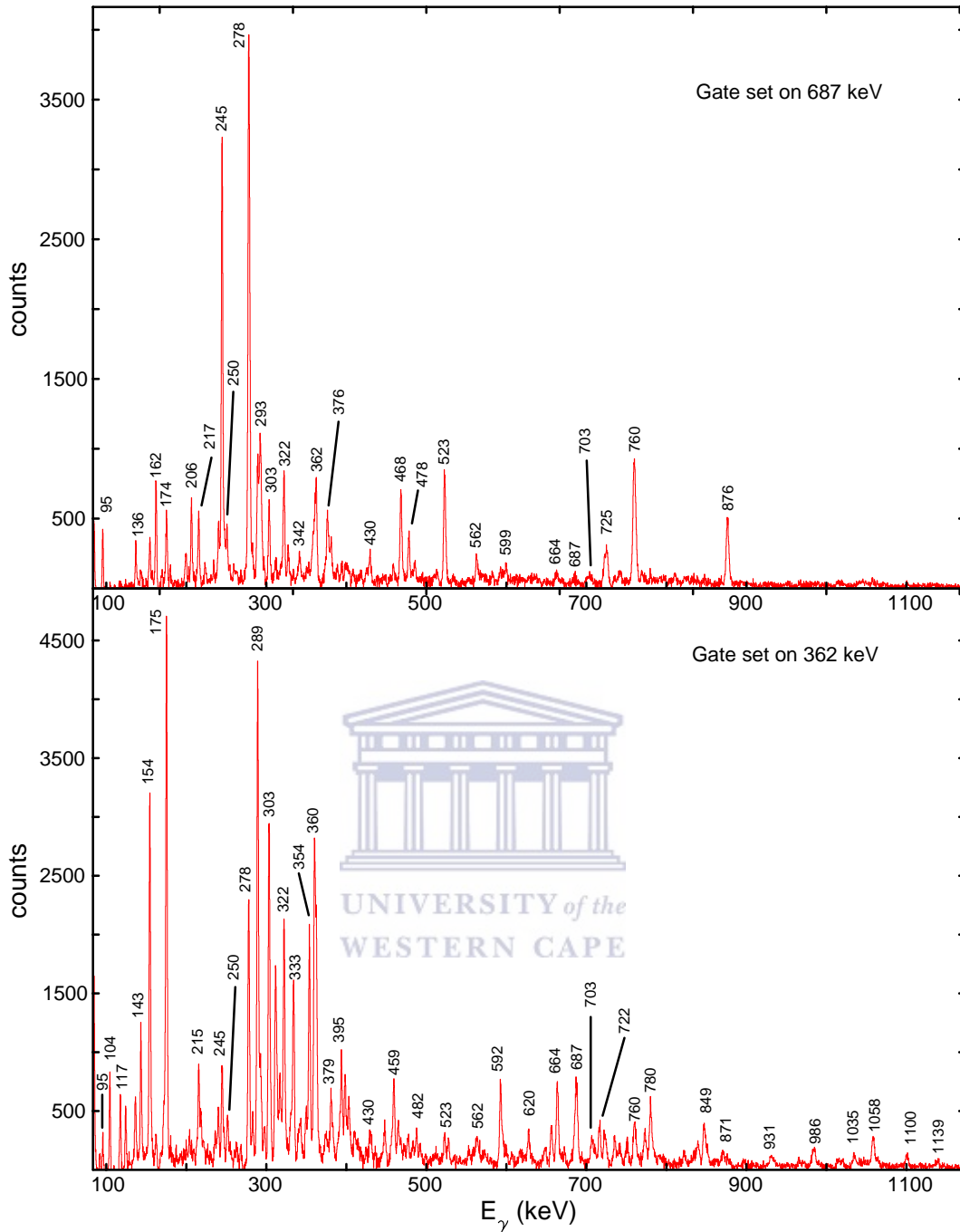
Figure 5-8: The γ – ray coincidence spectra gated on the (a) 687 keV transition (top panel) and (b) 362 keV transition (bottom panel).

Band 4 and structure A.

Band 4 is based on the $I^\pi = 12^{(+)}$ level and is composed of only a few transitions. The band extends up to $I^\pi = (17)$ which is a tentative level. The transitions in band 4 are

shown in Figure 5.7 and are marked with stars. The transitions underneath band 4 called structure A are very week and are placed tentatively in the level scheme. Some of them are shown in the spectra gated on the 342 and 303 keV transitions in Figure 5.10. The 459 keV transition initially placed in band 1 by a previous study [Kre79] is now placed in structure A.
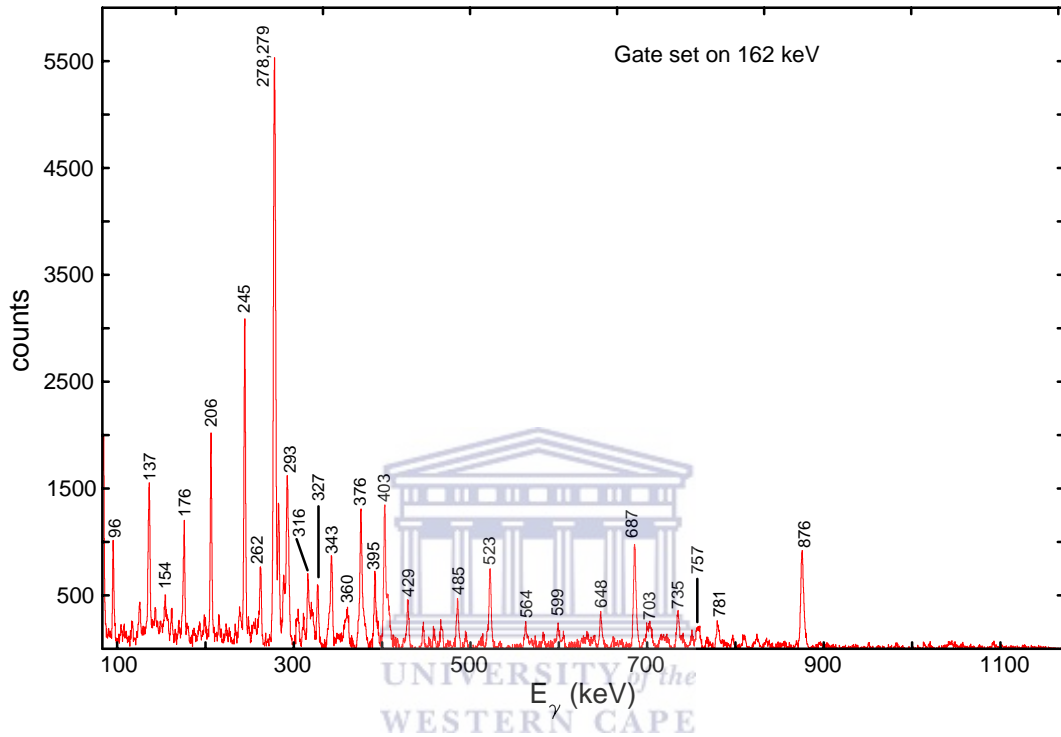
Figure 5-9: The γ - ray coincidence spectrum gated on the 162 keV transition. All the γ - rays seen in coincidence with the gate in both panels are labeled with their respective energies. The spectrum shows the coincidences of the transitions in band 3.
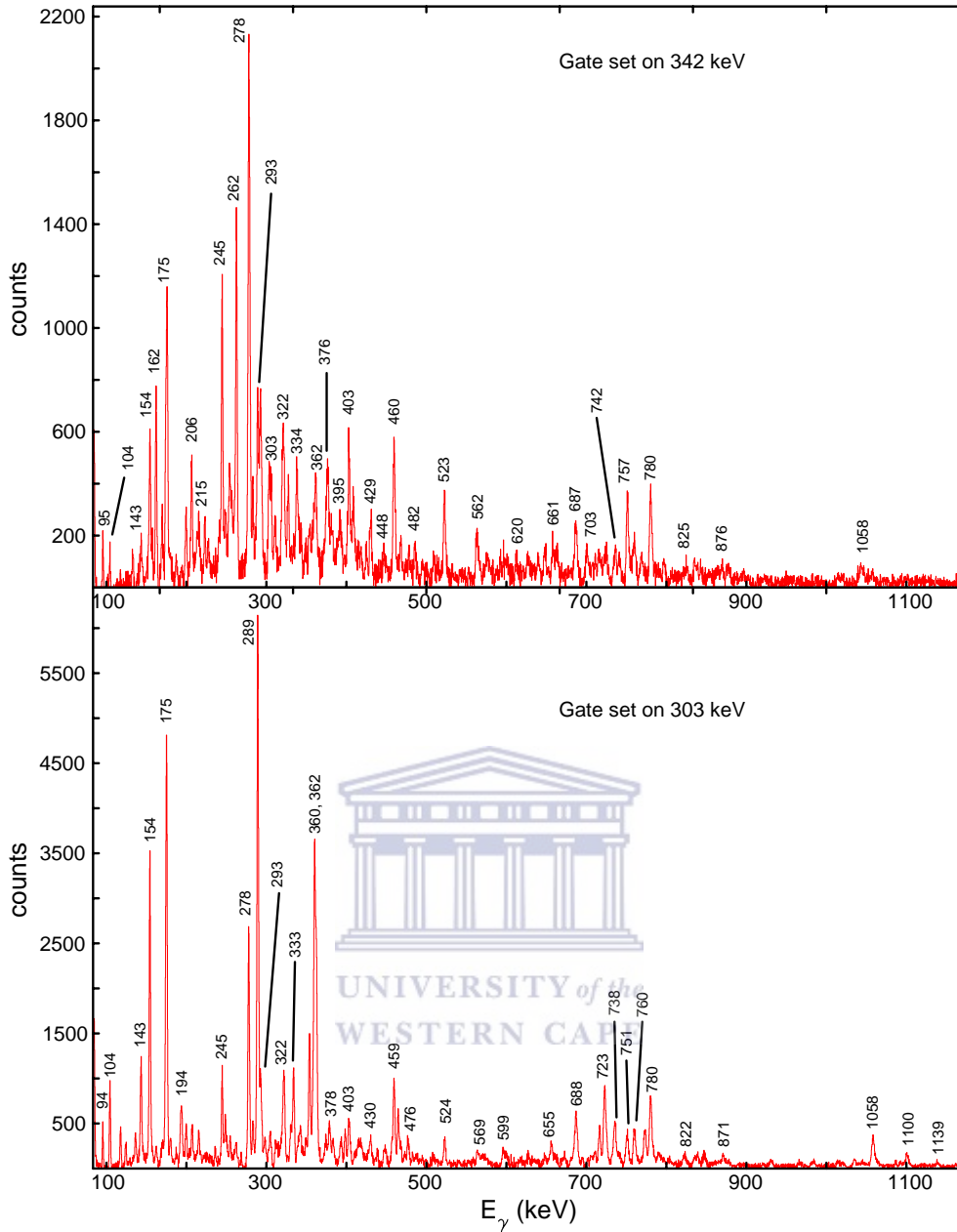
Figure 5-10: The γ – rays coincidence spectra gated on the (a) 342 keV transition (top panel) and (b) 303 keV transition (bottom panel).

5.2 ^{194}Tl DCO (Directional Correlations from Orientated states)

The R$_{DCO}$ for a number of transitions with known multipolarities in ^{194}Tl [Kre79] were measured and compared with the R$_{DCO}$ for the new transitions. Average R$_{DCO}$ values of 0.48 ± 0.03 and 0.83 ± 0.08 were obtained for the stretched dipole (∆I = 1) and the

stretched quadrupole ($\Delta I = 2$) transitions respectively and are marked by the dotted line in Figure 5.11. The results of the R_{DCO} determined for the ^{194}Tl transitions are given in Table 5.1 and depicted in Figure 5.11.

Table 5.1: Table of the DCO ratios calculations.

Energies	Gate 104	Gate 154	Gate 187	Gate 245	Gate 278	Gate 289	Gate 468	Gate 876	Gate 1058	DCO Final	Assignment
42											
45.2				0.54(10)	0.41(9)	0.58(14)	0.56(12)			0.52(11)	D
75.8		0.52(4)				0.58(7)				0.55(6)	D
78.7	0.44(13)			0.52(15)	0.48(8)			0.51(11)		0.48(12)	D
91.7	0.62(9)	0.53(11)	0.59(9)							0.54(10)	D
95.7	0.52(6)	0.64(13)	0.48(25)	0.46(7)	0.51(8)	0.32(11)	0.43(4)	0.62(7)	0.54(8)	0.46(10)	D*
104.4		0.42(9)			0.61(6)	0.43(9)			0.56(8)	0.51(8)	D
124.5	0.47(12)	0.48(10)	0.64(9)		0.58(7)	0.52(10)				0.53(12)	D
136.4				0.53(7)	0.55(10)		0.58(8)			0.55(8)	D
143.2	0.42(6)	0.55(9)	0.68(14)		0.48(6)	0.34(9)			0.48(10)	0.54(9)	D
154.2	0.54(14)				0.47(11)	0.43(13)	0.52(9)		0.49(7)	0.49(11)	D
157.6	0.54(12)		0.54(7)		0.51(9)					0.53(9)	D
162.1	0.49(10)			0.54(7)	0.49(12)			0.45(6)		0.49(9)	D
174.3		0.49(8)	0.46(11)							0.48(10)	D
175.5 Band 2	0.45(9)	0.47(2)				0.51(2)			0.53(7)	0.49(2)	D
176.3 Band 3				0.53(12)	0.56(6)					0.55(9)	D
186.8					0.51(4)				0.56(10)	0.54(7)	D
206.4				0.53(7)	0.47(11)		0.43(9)			0.51(9)	D
215.3				0.54(7)	0.48(11)		0.39(0.17)			0.47(12)	D
226.4			0.55(12)	0.34(9)	0.45(13)				0.64(6)	0.49(10)	D
240.3				0.44(6)	0.51(5)		0.52(9)			0.48(7)	D
244.9					0.51(8)		0.48(10)	0.49(6)		0.49(8)	D *
262.4				0.58(13)	0.47(8)					0.53(11)	D
277.8 Band 1	0.44(8)	0.53(4)	0.46(6)	0.47(6)	0.50(7)	0.54(4)	0.45(6)	0.54(9)	0.52(4)	0.49(6)	D *
277.9 Band 3				042(8)	0.46(7)			0.48(10)		0.45(8)	D
282.9+282.9				0.46(9)	0.54(5)		0.49(7)			0.50(7)	D *
289.3	0.45(8)	0.42(12)			0.48(6)				0.51(5)	0.47(8)	D *
291.4				0.58(13)	0.42(11)		0.48(5)			0.49(10)	D
293.4	0.42(10)	0.48(4)	0.61(7)	0.58(9)	0.62(2)	0.55(3)	0.48(5)	0.64(9)	0.58(7)	0.55(6)	D *
303.8	0.41(5)	0.38(8)			0.42(11)	0.45(6)				0.42(8)	D
320.1	0.38(8)	0.43(6)				0.42(11)			0.46(9)	0.42(9)	D
321.8 Band1				0.56(13)			0.48(7)			0.52(10)	D
322.4 Band2	0.47(7)	0.44(12)				0.51(5)			0.49(4)	0.48(7)	D
323.2 Band 4			0.51(7)							0.51(7)	D
327.4				0.56(9)	0.49(11)			0.52(7)		0.52(9)	D
333.5	0.49(11)	0.53(6)			0.42(5)	0.56(9)				0.50(8)	D
342.9	0.51(10)	0.57(12)			0.41(9)	0.45(10)				0.52(11)	D
343.7 Band 3				0.54(7)	0.62(11)					0.58(9)	D

Energies	Gate 104	Gate 154	Gate 187	Gate 245	Gate 278	Gate 289	Gate 468	Gate 876	Gate 1058	DCO Final	Assignment
354.1	0.47(6)	0.51(11)			0.52(7)	0.43(9)			0.48(12)	0.48(9)	D
360.4	0.29(13)	0.64(5)				0.45(7)			0.51(10)	0.47(9)	D
361.8 Band 1				0.52(12)			0.42(8)			0.47(10)	D
362.6+362.6	0.64(7)	0.54(11)				0.51(9)			0.48(6)	0.52(8)	D
376.4				0.53(7)	0.47(4)			0.43(11)		0.48(10)	D
379.8				0.64(11)	0.46(5)		0.58(9)			0.56(8)	D
395.4				0.45(18)	0.52(16)			0.53(15)		0.51(16)	D
398.2		0.43(11)			0.48(14)	0.54(10)			0.51(16)	0.49(13)	D
403.6				0.45(4)	0.47(3)		0.43(6)	0.53(8)		0.47(5)	D *
414.7	0.57(12)	0.51(5)	0.42(10)			0.36(5)				0.47(9)	D
429.8				0.48(6)	0.53(12)			0.55(12)		0.52(10)	D
430.9	0.49(10)	0.54(15)	0.68(19)			0.47(15)				0.55(15)	D
448.3	0.46(26)	0.64(13)			0.49(18)	0.54(13)			0.47(15)	0.52(17)	D
459.8	0.47(12)	0.41(7)				0.58(9)				0.49(9)	D *
464.8	0.66(16)	0.83(14)			0.84(13)				0.78(11)	0.78(14)	Q
468.4				0.49(6)	0.43(6)					0.46(6)	D
478.3				0.41(12)	0.44(9)		0.48(14)			0.44(12)	D
482.2					0.42(16)	0.48(10)			0.45(13)	0.45(13)	D
485.4				0.79(8)	0.84(8)		0.82(11)			0.82(9)	Q
522.7							0.83(6)	0.78(8)		0.81(7)	Q *
562.8				0.57(2)	0.75(10)		0.74(8)			0.68(10)	Q
569.6	0.82(16)			0.78(12)	0.84(18)					0.81(15)	Q
582.7					0.86(6)					0.82(6)	Q
592.7		0.76(10)			0.81(8)		0.76(6)		0.84(13)	0.79(9)	Q
620.7	0.76(8)				0.80(11)		0.78(6)			0.78(8)	Q
648.3					0.92(9)					0.92(9)	Q*
655.9		0.91(9)			0.78(15)	0.81(10)			0.78(11)	0.82(11)	Q
664.2	0.74(11)	0.76(10)			0.83(12)					0.77(11)	Q
686.5	0.72(8)	0.79(6)				0.86(6)			0.85(13)	0.81(8)	Q *
685.2+687.9		0.82(5)		0.83(8)	0.91(6)			0.88(9)		0.86(7)	Q
703.8	0.82(9)									0.82(9)	Q
716.7		0.77(9)			0.82(7)	0.78(8)			0.76(6)	0.78(8)	Q
722.8	0.51(10)	0.81(18)			0.92(9)	0.84(11)				0.77(12)	Q
725.8				0.89(15)	0.84(10)		0.82(18)			0.85(14)	Q
740.0				0.85(17)	0.76(12)		0.77(13)			0.79(14)	Q *
757.2				0.84(18)	0.92(16)					0.88(17)	Q
760.8 Band 2	0.84(13)	0.78(17)		0.83(15)			0.82(34)		0.77(13)	0.81(18)	Q
769.7							0.94(9)			0.94(9)	Q
773.4	0.78(17)	0.61(6)	0.63(21)			0.77(6)				0.69(13)	Q
780.2	0.78(5)	0.83(11)	0.68(12)			0.63(9)				0.92(9)	Q
781.1				0.42(8)						0.42(8)	D
790.6	0.66(15)	0.66(13)	0.64(18)		0.73(15)	0.94(12)				0.73(15)	Q
822.6	0.77(21)	0.83(26)								0.80(24)	Q
825.2					0.84(13)	0.78(11)				0.81(12)	Q
871.2	0.83(19)	0.69(27)			0.91(25)					0.81(14)	Q
876.4					0.61(6)					0.61(6)	D

Energies	Gate 104	Gate 154	Gate 187	Gate 245	Gate 278	Gate 289	Gate 468	Gate 876	Gate 1058	DCO Final	Assignment
1058.3	0.69(7)	0.69(5)	0.91(11)			0.78(9)				0.62(8)	D
1100.8		0.51(14)	0.56(24)			0.51(16)				0.53(18)	D
1138.6	0.73(28)	0.52(13)	0.75(27)							0.66(22)	D
1162.6											
1250.4											

* Indicate the previously known transitions

The numbers inside the brackets represent the systematic errors

Q = Quadrupole transitions and D = Dipole transitions
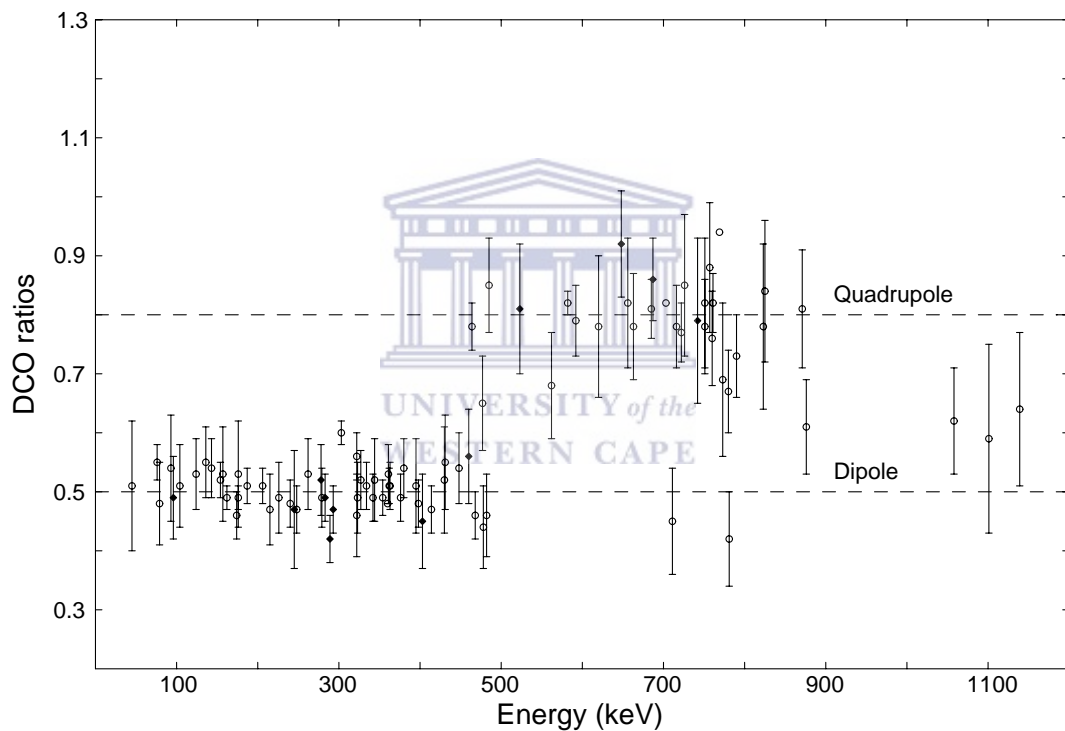
Figure 5-11: The DCO ratios for the γ - ray transitions. Open – circles are associated with the new transitions and filled solid diamonds correspond to the previously known transitions.

The R_{DCO} measurements for the ^{194}Tl transitions indicate that the level scheme presented in Figure 5.2 include sequences of stretched dipole with associated stretched quadrupole (cross – over) transitions.

CHAPTER 6

DISCUSSION

The present chapter details the interpretation of the experimental data in relation to the theoretical predictions of the Total Routhian Surface (TRS) and the Cranked Shell Model (CSM) calculations. The experimental routhians, band crossing frequencies, signature inversion and aligned angular momenta are compared with the theoretical predictions for band 1. The results were also compared with the values obtained for the neighboring [193]Hg isotone. In general reasonably good agreement between the experimental and the predicted values is obtained. These theoretical models however fail to predict the signature inversion observed in the experimental data for band 1.

6.1   Experimental bandcrossings and alignments

In order to compare the properties of the observed rotational bands to the results of our CSM calculations, the experimental quantities have to be transformed into the rotating frame [Rev92].
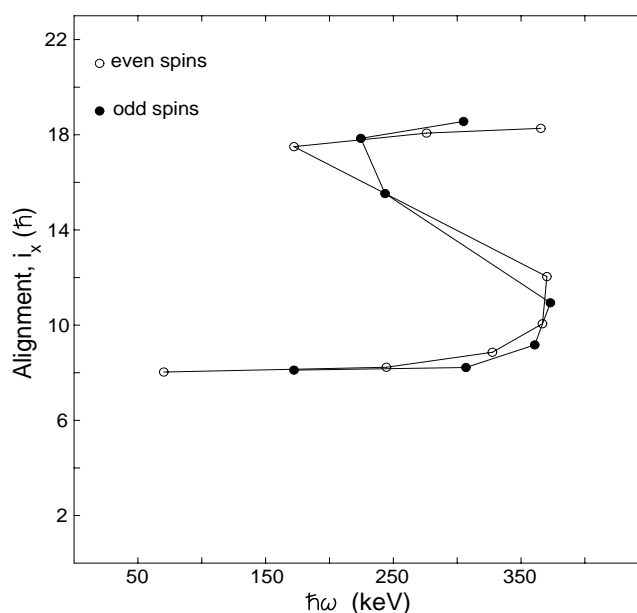
Figure 6-1: The experimental alignment as a function of the rotational frequency for the $\pi h_{9/2} \otimes \nu i_{13/2}$ yrast band of the doubly – odd [194]Tl isotope.

The Harris expansion $I_x^{ref} = J_0\omega + J_1\omega^3$, with parameters $J_0 = 8$ $\hbar^2$ MeV^{-1} and $J_1 = 40$ $\hbar^4$ MeV^{-3} was used for the ^{194}Tl isotope. These parameters are chosen to be the same as those used for the neighboring even – odd ^{193}Hg isotone [Hüb86]. The configuration previously assigned to band 1 is $\pi h_{9/2} \otimes \nu i_{13/2}$ configuration with $\Omega_p = 9/2$. Back bending occurs in band 1 between the levels with spins of I $\sim 16^- \rightarrow 20^-$. We suggest that it is due to the alignment of a pair of $\nu i_{13/2}$, using a comparison with the neighboring nuclei, i.e. ^{193}Tl, ^{197}Tl, and the neighboring oblate Hg [Hüb85] and Au nuclei. The experimental alignments for band 1 are plotted on Figure 6.1 and show a gain in the alignment of $\Delta i = 10$ $\hbar$ for band 1. This value differs slightly from the $\Delta i = 9.2$ $\hbar$ corresponding to the ground – state band in ^{193}Hg.

6.2   Routhians and signature splitting

The experimental quasiparticle energies in a rotating frame (routhians) for the yrast band of ^{194}Tl as a function of the rotational frequency are shown in the Figure 6.2. As seen in Figure 6.2 the band crossing frequency is $\hbar\omega = 0.3$ MeV.
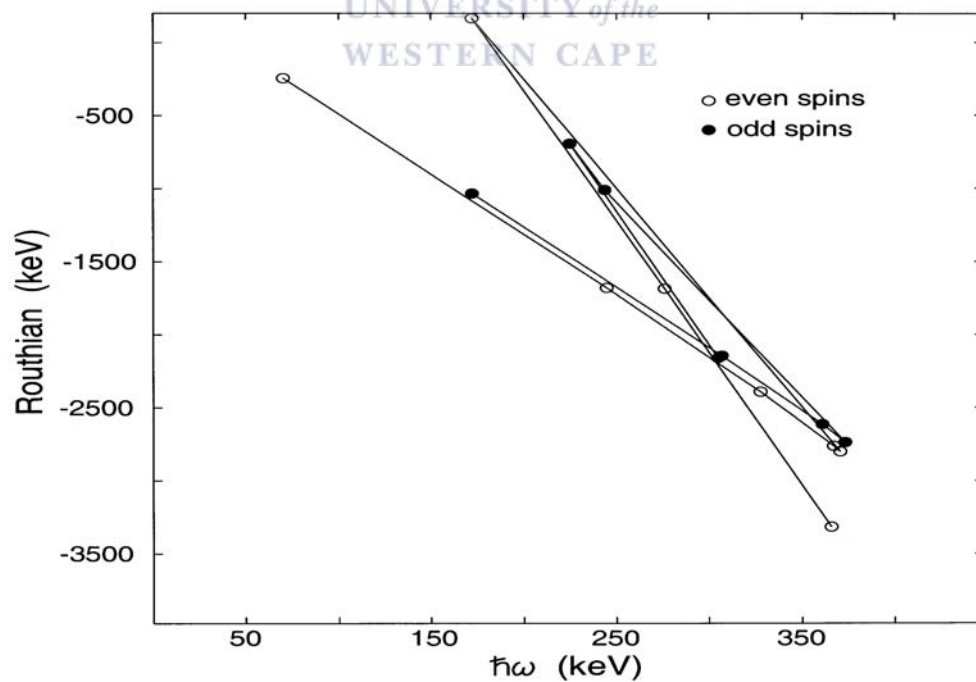
Figure 6-2: Experimental routhians extracted for the band 1 in ^{194}Tl nuclei as a function of the rotational frequency. The Harris parameters of: $J_0 = 8\hbar^2 MeV^{-1}$ and $J_1 = 40\hbar^4 MeV^{-3}$ [Hüb86] were used as reference.

This result is compared with the measured value in the ^{193}Hg isotone, where the same Harris parameters $J_0 = 8$ $\hbar^2$ MeV^{-1} and $J_1 = 40$ $\hbar^4$ MeV^{-3} were used. The band crossing frequency found in the yrast band of ^{193}Hg is $\hbar\omega_c = 0.265$ MeV. Band 1 also exhibits a large signature splitting, called in this case a signature inversion, because, the

$\alpha_{f,p-n} = \alpha_{f,p} + \alpha_{f,n} = \frac{1}{2} + \frac{1}{2} = 1$ favoured signature branch of the band lies higher

in energy than the $\alpha_{u,p-n} = \alpha_{f,p} + \alpha_{u,n} = \frac{1}{2} - \frac{1}{2} = 0$ unfavoured signature branch. The favored signatures for the $\pi h_{9/2}$ and $\nu i_{13/2}$ orbitals were calculated as follows:

$$\alpha_f\left(\nu i_{13/2}\right) = \frac{1}{2}(-1)^{j_n - \frac{1}{2}} = \frac{1}{2}(-1)^{\frac{13}{2} - \frac{1}{2}} = \frac{1}{2} \tag{6.1}$$

$$\alpha_f\left(\pi h_{9/2}\right) = \frac{1}{2}(-1)^{j_p - \frac{1}{2}} = \frac{1}{2}(-1)^{\frac{9}{2} - \frac{1}{2}} = \frac{1}{2} \tag{6.2}$$

$$\alpha_f\left(\pi h_{9/2} \otimes \nu i_{13/2}\right) = \frac{1}{2}(-1)^{j_n - \frac{1}{2}} + \frac{1}{2}(-1)^{j_p - \frac{1}{2}} = \frac{1}{2} + \frac{1}{2} = 1 \tag{6.3}$$
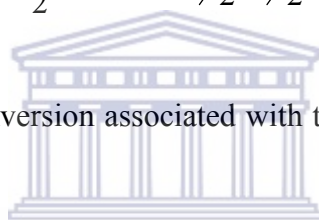
The experimental signature inversion associated with the oblate $\pi h_{9/2} \otimes \nu i_{13/2}$ band is shown in Figure 6.3.
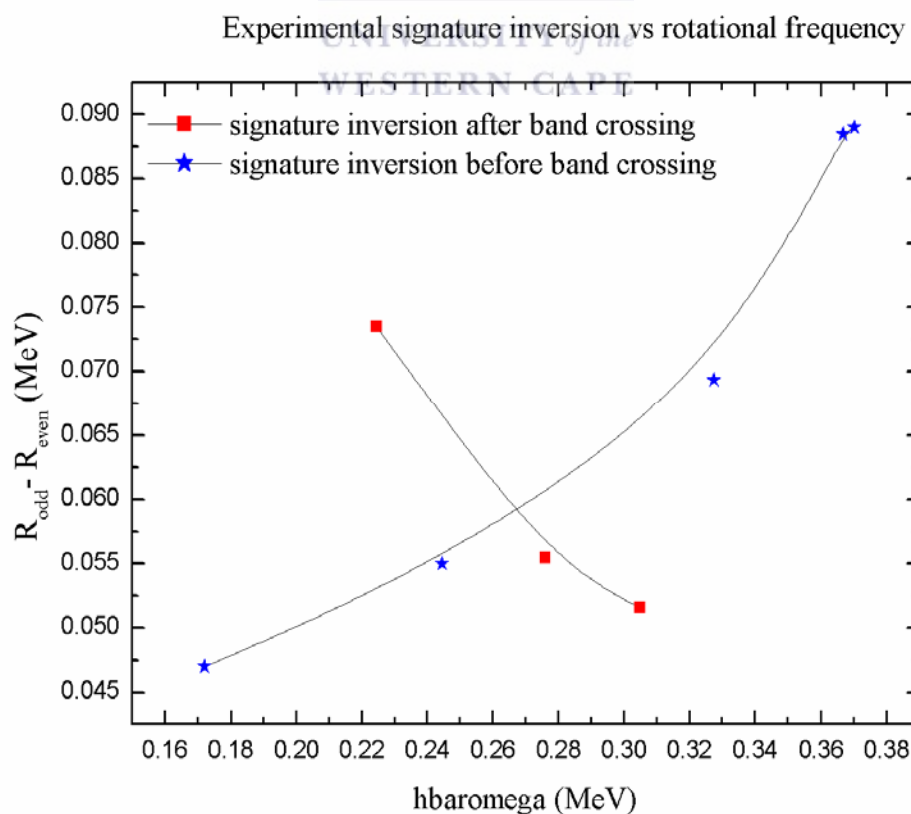
Figure 6-3: Plot of the experimental signature inversion before and after the band crossing.

66

6.3   Theoretical calculations

6.3.1   Total Routhian Surface calculations

The relevant nuclear shape parameters obtained as a function of both the rotational frequency and the quasiparticle configurations [Naz85] can be predicted by the total routhian surface calculations (TRS). The shape parameters for ^{194}Tl presented in the following discussion have been extracted from total routhian surfaces (TRS) calculations [Wys90].
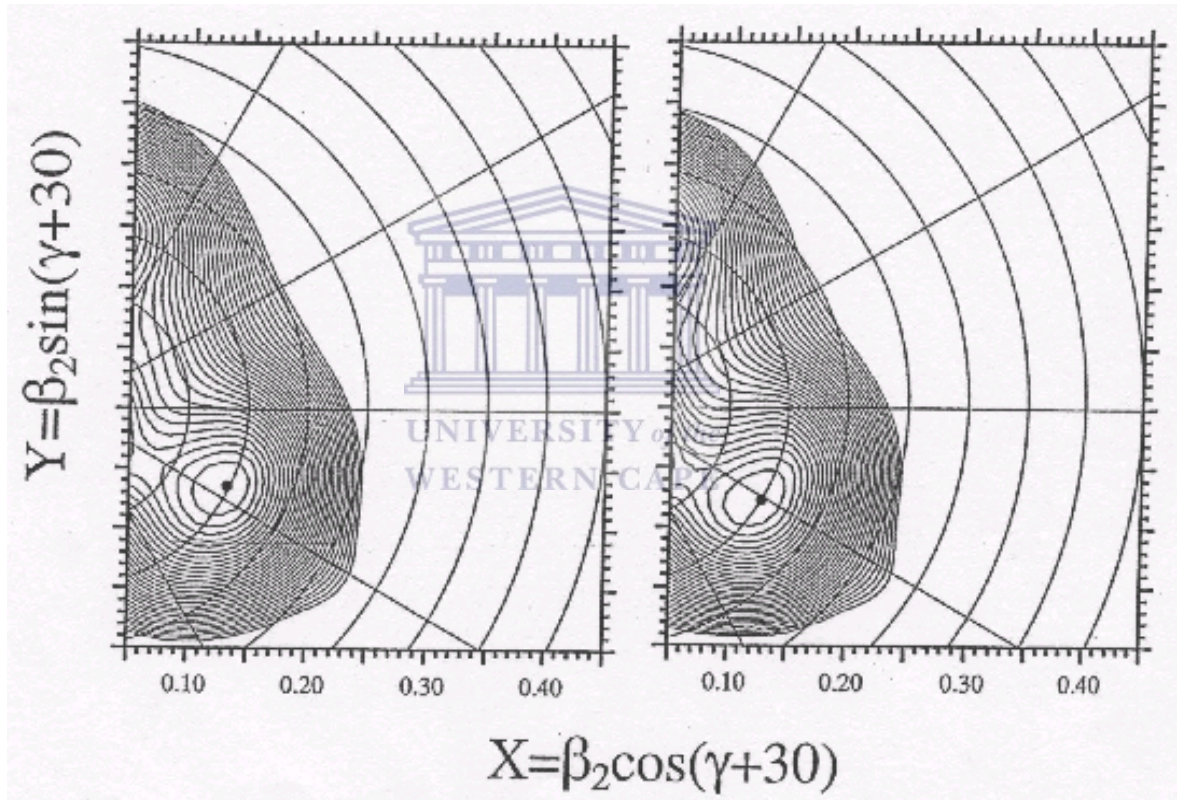
Figure 6-4: Total routhian surfaces for band 1(eA band 8⁻) in ^{194}Tl calculated for configuration. The left panel is calculated at $\hbar\omega = 0.127$ MeV which is before the $\nu i_{13/2}$ band crossing and shows a minimum at $\beta_2 = 0.148$, $\beta_4 = -0.022$ and $\gamma = -55.9$. The right panel is calculated at $\hbar\omega = 0.206$ MeV (after the $\nu i_{13/2}$ bandcrossing) and shows a minimum at $\beta_2 = 0.150$, $\beta_4 = -0.021$ and $\gamma = -61.1$.

The TRS calculations were performed in order to obtain three equilibrium deformation parameters of nuclear shape i.e. β_2, γ and β_4. The surface deformation

parameters $\hat{\beta}$ = (β_2, γ, β_4) and the BCS (Baedeen, Cooper and Schrieffer) field parameters Δ_p and Δ_n for protons and neutrons are treated as variation parameters. Examples of total routhian surfaces in ^{194}Tl for quasiparticle configurations with negative and positive parity are shown in Figures 6.4 and 6.5. The black dot surrounded by regular contour line shows the potential energy minimum and also represents the equilibrium nuclear shape, i.e. the shape that the nucleus possesses in order to be in the lowest possible total energy. The surface energy of the nucleus has been minimized with respect to the hexadecapole degree of freedom and projected in the (β_2, γ) − plane. More results from the TRS calculations for band 1 are listed in table 6.1.
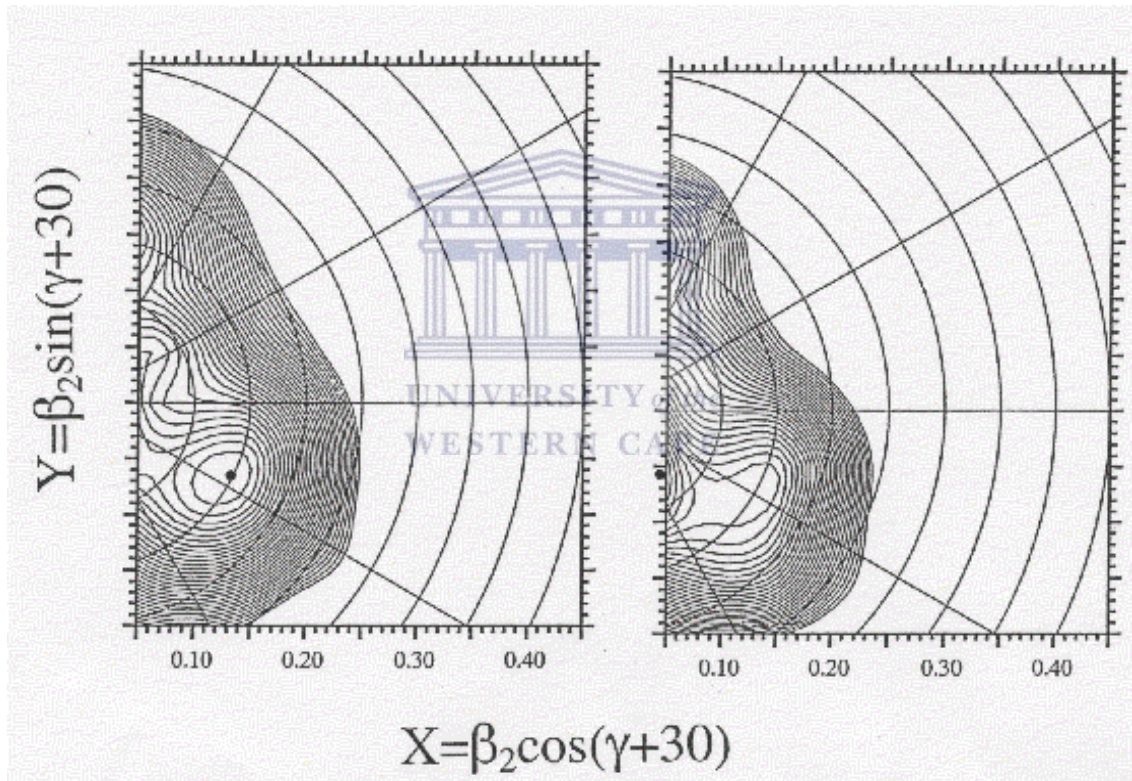
Figure 6-5: Total routhian surfaces for band 1(fA band 9') in ^{194}Tl calculated for configuration before and after the $\nu i_{13/2}$ alignment. The left panel is before the bandcrossing corresponds to $\hbar\omega$ = 0.049 MeV with the deformation parameters of β_2 = 0.148, β_4 = -0.021 and γ = -56.0 and the right panel is after the bandcrossing corresponds to $\hbar\omega$ = 0.206 MeV with the deformation parameters of β_2 = 0.072, β_4 = -0.001 and γ = -82.4.

The calculations predict a minimum on the total routhian surface for the ^{194}Tl. This minimum is shown in Figures 6.4 and 6.5 for rotational frequencies of $\hbar\omega$ = 0.127 (or

0.049) MeV and $\hbar\omega$ = 0.206 MeV. It corresponds to a small aligned angular momentum below the bandcrossing.

Furthermore the calculations also predict that the oblate minimum on the total routhian surface for ^{194}Tl shown in the Figures 6.4 and 6.5 persists for rotational frequencies of 0.049 MeV < $\hbar\omega$ < 0.206 MeV and also at higher $\hbar\omega$ above the bandcrossing as seen in table 6.1. The shape parameters given above have been used as input parameters for the cranked shell model (CSM) calculations, which provide a detailed insight into the structural properties of this nucleus.

Table 6.1: The deformation parameters of the ^{194}Tl nuclei, calculated with TRS for band 1. The even and odd – spin levels from band 1 form two E2 sequences, which correspond to eA and fA configurations respectively. In this notation the parity and signature quantum number are as follows: e (-, -1/2), A (+, +1/2), f (-, +1/2) and A (+, +1/2)

	fA band						
$\hbar\omega$ (MeV)	β_2	γ	β_4	E'(MeV)	E_{abs}(MeV)	I_p	I_n
0.049	0.146	-56.4	-0.021	-3.48	-3.48	0.26	6.57
0.088	0.147	-56.1	-0.0213	-4.11	-3.43	0.63	7.11
0.127	0.148	-55.9	-0.022	-4.43	-3.34	0.99	7.6
0.166	0.15	-54.6	-0.0237	-4.77	-3.16	1.36	8.3
0.206	0.15	-61.1	-0.0212	-5.28	-1.64	1.46	16.26
0.245	0.151	-61.3	-0.0215	-6.09	-1.25	1.78	18.01
0.284	0.146	-63.3	-0.0201	-6.97	-1.24	1.99	18.21
0.323	0.151	-57.9	-0.0238	-7.88	-0.73	2.5	19.65
0.362	0.15	-58.4	-0.0253	-8.85	-0.08	2.88	21.35

	eA band						
$\hbar\omega$ (MeV)	β_2	γ	β_4	E'(MeV)	E_{abs}(MeV)	I_p	I_n
0.049	0.148	-56	-0.0209	-3.8	-3.47	0.19	6.58
0.088	0.149	-55.4	-0.0213	-4.09	-3.42	0.43	7.12
0.127	0.15	-54.6	-0.0221	-4.4	-3.33	0.83	7.63
0.166	0.152	-53.2	-0.024	-4.75	-3.15	1.3	8.29
0.206	0.152	-56.2	-0.0233	-5.22	-1.96	1.41	14.46
0.245	0.152	-56.4	-0.0229	-6.01	-0.96	2.38	18.25
0.284	0.155	-59	-0.0203	-6.95	-0.46	4.35	18.51

6.3.2   Cranking model interpretation

The cranked shell model (CSM) was described in details by Bengtsson and Frauendorf [Ben79]. The CSM calculations were performed for ^{194}Tl nucleus because

they may offer a possible explanation for the apparent band crossing suggested by the data. In the following we first give a few details about the calculations and then present an interpretation of band 1 within the CSM and a comparison between calculated and experimental quantities.

6.3.3 CSM calculations

In order to obtain a deeper understanding of the band properties in ^{194}Tl, we have performed cranked shell model (CSM) calculations. CSM calculations were carried out utilizing a Woods Saxon potential with universal parameters. The deformation parameters have been extracted at the minimum of the potential energy, with the aid of the TRS calculations. The experimental routhians and alignments obtained for the negative – parity E2 sequence of band 1 in ^{194}Tl are presented as a function of the rotational frequency in Figures 6.2 and 6.1, respectively. The even and odd – spin sequences of band 1 correspond to eA and fA configurations respectively, e.g the $h_{9/2}$ proton (with $\Omega_p = 9/2$ projection on the symmetry axis) is coupled to the neutron $i_{13/2}$ orbital.
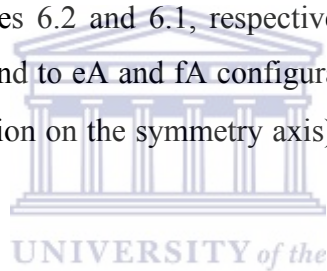
Table 6.2: The deformation parameters for eA and fA configurations extracted from the TRS calculations.

Deformation parameters for eA band (8⁻)						
β_2	β_4	γ	Δ_n	Δ_p	λ_n	λ_p
0.150	-0.022	-54.8	0.9946	0.5162	-8.7668	-3.2613
Deformation parameters for fA band (9⁻)						
β_2	β_4	γ	Δ_n	Δ_p	λ_n	λ_p
0.148	-0.022	-55.8	0.9999	0.5168	-8.7699	-3.2463

Figure 6.8 shows the quasiparticle routhians for neutrons and protons plotted as a function of the rotational frequency for the deformation parameters obtained from the TRS calculations for eA configuration. The first band crossing as seen in Figure 6.8 is AB crossing and occurs at $\hbar\omega = 0.2$ MeV. This AB crossing is blocked because the

70

routhian A is occupied. The second band crossing is a BC crossing and occurs at ħω = 0.25 MeV and is not blocked. Therefore the predicted band crossing frequency for band 1 in the ^{194}Tl nucleus is ħω = 0.25 MeV.
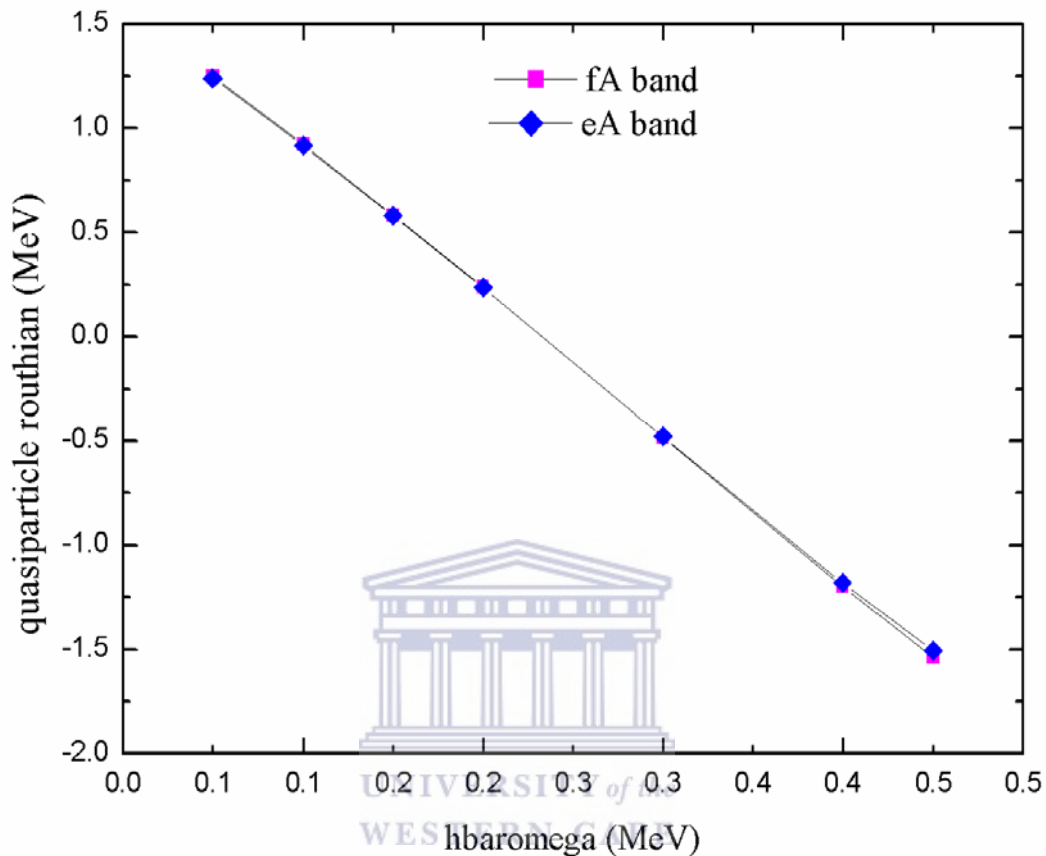
Figure 6-6: A plot of quasiparticle routhian versus rotational frequency. Calculated quasiparticle routhians for fA and eA sequences of band indicating. Band fA (favored) is lying at lower energy than band eA (unfavored).

The calculated gain in the alignment for this bandcrossing is i_{BC} = 8.86 ħ. Experimental signature inversion was observed in band 1 as shown in Figure 6.3. However CSM was unable to predict it. Figure 6.3 shows the experimental signature inversion before and after the band crossing. The experimental signature inversion is large compared to the theoretical calculations, as shown in Figure 6.7.

Figure 6-7: A plot of signature splitting and inversion of fA and eA bands vs rotational frequency. Calculated signature splitting and inversion for band 1 in ^{194}Tl.Signature splitting

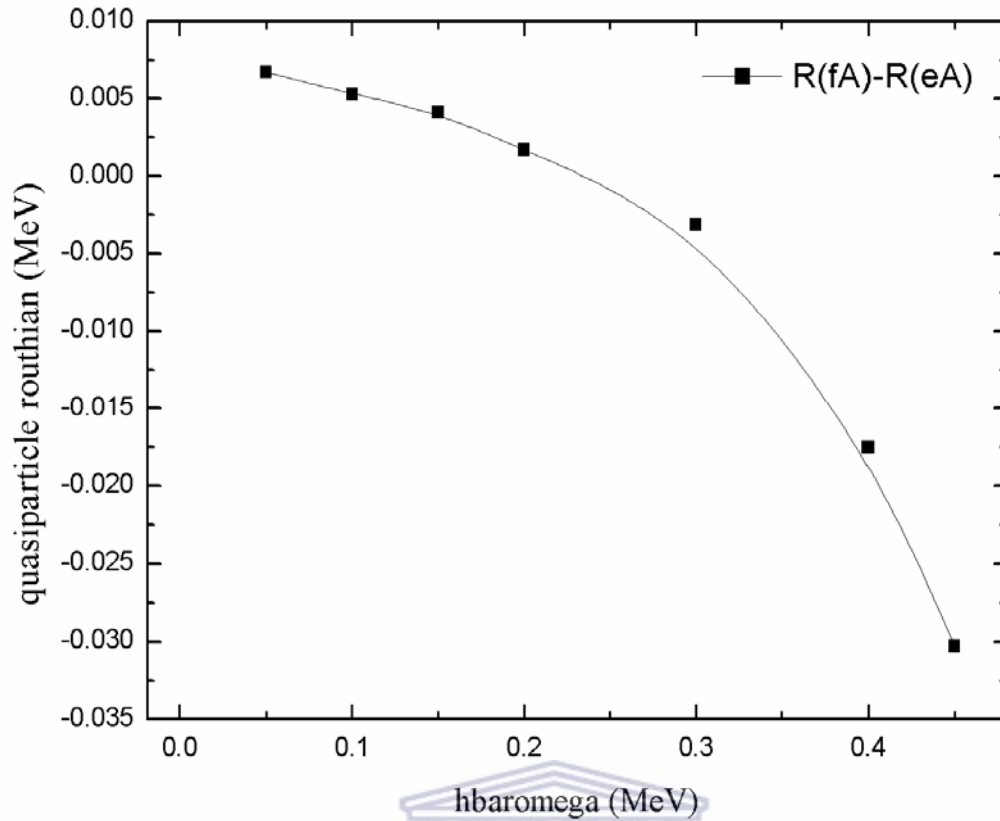*Table 6.3: The data extracted from CSM, which predicts signature splitting. Quasiproton routhians R (f), quasineutron routhian R (A) and the total quasiparticle routhian (R (f) + R (A) = R (fA)) of the 9$^-$ sequence of band 1. The quasiproton routhian R (e) and the total quasiparticle routhian (R (e) + R (A) = R (eA)) of the 8$^-$ sequence of band 1.*

		Band fA			Band eA		
ℏω (MeV)	R (f) MeV	R (A) MeV	R (fA) MeV	R (e) MeV	R (A) MeV	R (eA) MeV	R (fA) -R (eA) MeV
0	0.5429			0.5396			
0.05	0.537	0.7099	1.2469	0.5337	0.7065	1.2402	0.0067
0.1	0.5197	0.4026	0.9223	0.5165	0.4005	0.917	0.0053
0.15	0.4914	0.0936	0.585	0.4885	0.0924	0.5809	0.0041
0.2	0.4531	-0.2155	0.2376	0.4507	-0.2148	0.2359	0.0017
0.25	0.406			0.4046			
0.3	0.3523	-0.8343	-0.482	0.3528	-0.8317	-0.4789	-0.0031
0.35	0.2953			0.2993			
0.4	0.2415	-1.4403	-1.1988	0.2519	-1.4332	-1.1813	-0.0175
0.45	0.2029	-1.7393	-1.5364	0.2241	-1.7302	-1.5061	-0.0303

Figure 6.8: Quasiparticle routhians for neutrons plotted as a function of the rotational frequency of ^{194}Tl. *The calculations were done using* $\beta_2 = 0.148$, $\beta_4 = 0.022$ *and* $\gamma = -55.8$ *predicted by TRS for the eA configuration. The parity and signature* (π, α) *of the routhians are represented as follows: (+, +1/2) solid lines, (+,-1/2) dotted lines, (-,+1/2) dash – dotted lines and (-,-1/2) dashed lines.*
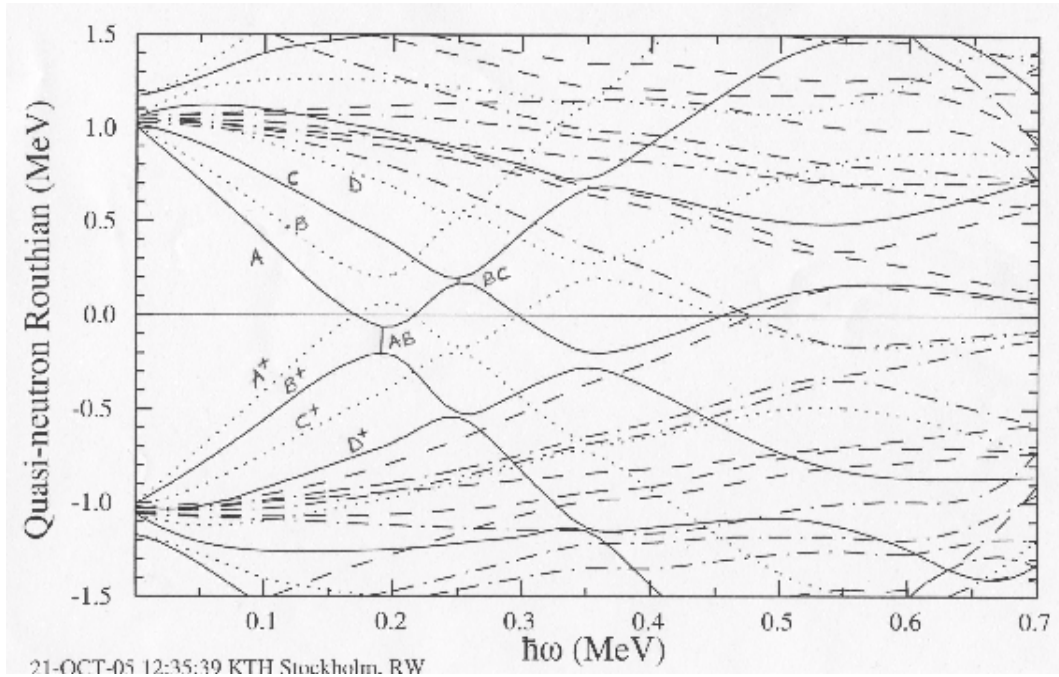

Figure 6-8: Quasiparticle routhians for protons plotted as a function of the rotational frequency of ^{194}Tl. *The calculations were done using* $\beta_2 = 0.148$, $\beta_4 = 0.022$ *and* $\gamma = -55.8$ *predicted by TRS for the eA configuration. The parity and signature* (π, α) *of the routhians are represented as follows: (+, +1/2) solid lines, (+,-1/2) dotted lines, (-,+1/2) dash – dotted lines and (-,-1/2) dashed lines.*
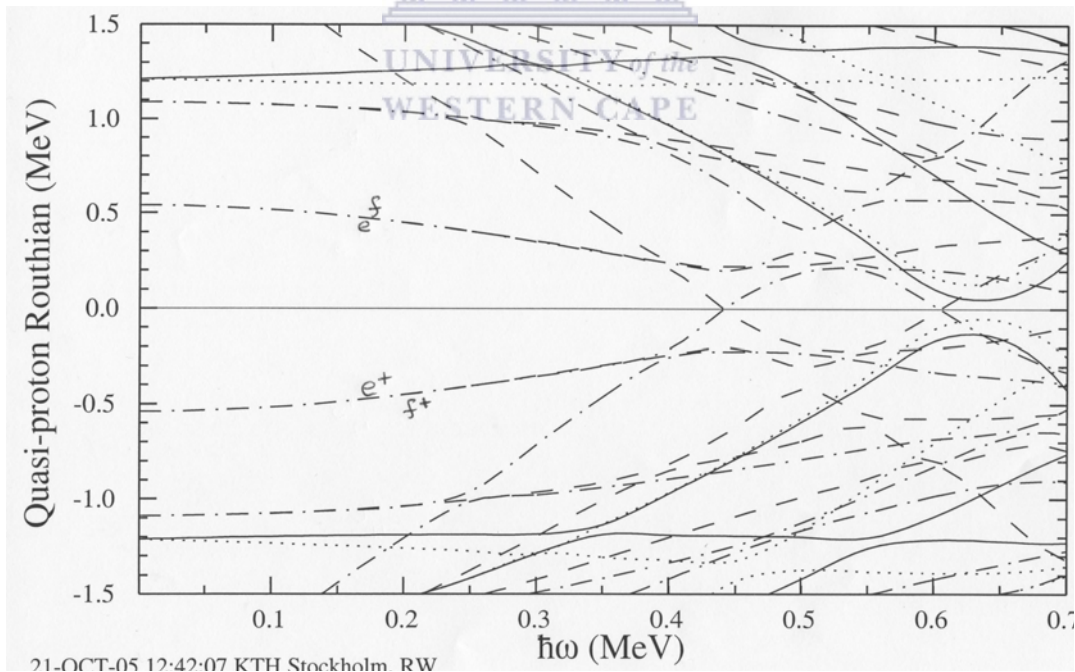
73

6.4   Comparison with experiment

A comparison with the experimentally measured band crossing frequency and gain in the alignment in the yrast band suggests that the first band crossing involves the alignment of an $i_{13/2}$ neutron pair.

Table 6.4: Comparison of experimental and calculated band crossing frequencies and alignments in ^{194}Tl and ^{193}Hg.

	Experimental results		CSM calculations	
	Band crossing frequency ħω (MeV)	Gain in alignment Δi (ħ)	Band crossing frequency ħω (MeV)	Gain in alignment Δi (ħ)
^{194}Tl	0.30	10	0.250	8.86
^{193}Hg	0.265	9.2	0.245	9.1

The band crossing frequency $\hbar\omega_{BC} \sim 0.25$ MeV predicted by CSM for the yrast band of ^{194}Tl is smaller in comparison with the experimentally measured $\hbar\omega \sim 0.30$ MeV. The gain in the alignment of about ~ 8.9 ħ predicted by CSM is smaller in comparison with the experimental measurement of ~ 10 ħ. Furthermore the results were compared with the neighboring ^{193}Hg isotone. The experimental band crossing frequency and alignment are 0.265 MeV and 9.2 ħ respectively, which differ slightly from the experimental data in ^{194}Tl. All results (experimental and CSM calculations) are summarized in table 6.3.

6.5   Summary and conclusions

The odd – odd nucleus ^{194}Tl has been populated following the bombardment of the ^{181}Ta target with ^{18}O projectiles. The level scheme of ^{194}Tl was extended to considerably higher spins by in – beam γ - ray spectroscopy using AFRODITE. Our data confirm the previously known level of ^{194}Tl [Kre79] however a few transitions were rearranged. The data analysis consists of analysis of the γ - γ coincidence

relationships and DCO (Directional Correlation of Oriented states) measurements. Several bands were observed for the first time in this nucleus and the previously known band 1 has been extended to higher excitation energies. The gap between 8^- and $(8 + \Delta I)^-$ levels in the previous level scheme was closed by placing a new transition of 45 keV. The $\pi h_{9/2} \otimes \nu i_{13/2}$ configuration and oblate nuclear deformation were assigned to band 1 in the previous studies of ^{194}Tl [Kre79]. Experimental band crossing frequency and gain in the alignment were both calculated. TRS and CSM models were used to interpret the data on band 1 in ^{194}Tl. The experimental and theoretical results for band 1 were compared with these in the neighboring ^{193}Hg isotone. Good agreement is obtained between the experimental and theoretical results for band 1 in ^{194}Tl isotope. The TRS and CSM models were unable to satisfactorily reproduce the experimentally observed signature inversion of the routhians of band 1. Experimentally a large signature inversion was observed, however the model shows small signature splitting. We adjusted the neutron pairing gap to 1 MeV, a value used in the neighboring Hg isotopes, but this did not influence significantly the signature splitting in band 1. This indicates that the models fail to predict the signature inversion in this band. The nucleus is explained very well by the theory; however the theory could not predict the splitting.
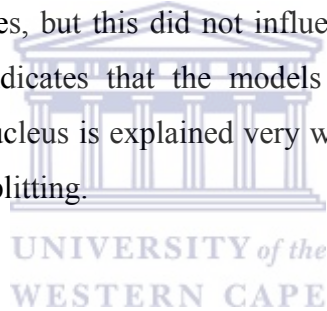
REFERENCES

[Bar87] J. Bardeen et al., Phys. Rev. 108, 1175 (1957)

[Ben79] R. Bengtsson and S. Frauendorf, Nucl. Phys. 8, 82 (1979)

[Ben83] R. Bengtsson and J. D. Garrett, Nordic winter school on Nuclear Physics,
   Hemsedal, Norway, April 10 – 21, 1983 to be published by word Scientific
   Publishing Co., Singapore in International Review of Nuclear Physics, vol. 2

[Ben85] R. Bengtsson and J.D. Garrett, In. Rev. Nucl. Phys. **1** World Scientific (1985)

[Boh36] N. Bohr, Nature 344 (1936) 137

[Boh75] A.Bohr and B. Mottelson, Nuclear Structure (Benjamin, Reading, MA,
   1975), Vol. II

[Bot87] A. H. Botha, S. J. Burger, J. J. Kritzinger, D. Reitmann, P. J. Celliers, P. M.
   Cronjie, H. N. Jungwirth, Proc. 11th Int. Conf. on Cyclotrons and their
   Applications, Ionics, Tokyo, 155 (1987).

[Dow00] D. Dowie and S. M. Mullins, *B.Sc (Physics) Vacation Project*, iThemba
   LABS, (unpublished), December (2000).

[Dra97] G. D. Dracoulis et al., Phys. G: Nucl. Part. Phys. 23 (1997) 1191 – 1202.

[Dud81] J. Dudek *et* al., Phys. Rev. C 23, 920 (1980)

[Dut87] Z. B. du Toit *et* al., Proc. 11th Int. Conf. on Cyclotrons and their Applications,
   Ionics, Tokyo, 109 (1987)

[Gav80] A. Gavron, Phys. Rev. C 23, 920 (1992)

[Gav93] A. Gavron, Computational Nuclear Physics 2, Nuclear Reactions, Springer –
   Verlag New York, Inc, 108 (1993).

[Gil95] Gordon Gilmore and John D. Hemingway, Practical Gamma – ray
   Spectrometry, (1995) Pages 199 and 202.

[Gre99] Paul Thomas Greenlees, PhD thesis, Department of physics,
   University of Liverpool (July 1999).

[Gue04] Elena Gueorguieva *et* al., Phys. Rev. C 69, 044320 – (2004)

[Gue99] Elena Atanassova Gueorguieva, PhD thesis, University Paris XI Orsary
   (June 1999)

[Har65] S.M. Harris, Phys. Rev. B 138 509 (1965)

[Hüb86] H. Hübel et al., Nucl. Phys. A 453 (1986) 344

[Ing54] D. R. Inglis, Phys. Rev. 96, 1059 (1954

[Ing55] D. R. Inglis, Phys. Rev. 97, 701 (1955)

[Kee00] Alex Keenan, PhD thesis, Department of physics, University of Liverpool
(December 1999).

[Kra73] K. S. Krane, R. M. Staffen and R. M Wheeler, Nuclear Data Table, 11, 351
(1973)

[Kra88a] Kenneth S. Krane, Introductory Nuclear Physics Copyright © 1988,
by John Wiley & Sons, Inc. Pages 430 – 433.

[Kra86] Kenneth S. Krane, Introductory Nuclear Physics Copyright © 1988, by John
Wiley & Sons, Inc. Page 213.

[Kre77] A.J. Kreiner *et* al., Nucl. Phys. A282 (1977) 243,

[Kre78] A.J. Kreiner *et* al., Nucl. Phys. A 308 (1978) 147,

[Kre79] A.J. Kreiner *et* al., Phys. Rev. C20 (1979) 2205,

[Kre80] A.J. Kreiner, Phys. Rev. C 22 (1980) 2570,

[Kre81] A.J. Kreiner *et* al., Phys. Rev. C23 (1981) 748,

[Lee97] I. Y. Lee *et* al., Phys. Rev. C, 56, Number 2, 56 (1997).

[Leo87] William R. Leo, Techniques for Nuclear and Particle Physics Experiments,
(1987), Page 242 and 269.

[Lil92] J.S. Lilley, Nuclear Physics Second Edition, Copyright © 1992, 1979 by John
Wiley & Sons Ltd, Baffins Lane, Chichester West Sussex PO19 1UD,
England. Pages 118, 136 – 142.

[Mab03] G.K. Mabala, PhD thesis, University of Cape Town (March 2000),

[Mih00] Lucian Mihailescu, A dissertation submitted to the Rheinischen Friedrich –
University Bonn, Mathematisch – Naturwissenschaftliches Fakultät,
2000 Page 11.

[Mye67] W.D. Myers and W. Swiatecki, Ark. Fys. 36, 343 (1967)

[Naz85] W. Nazarewicz *et* al., Nucl. Phys. A 435, 397 (1985)

[New98] R. T. Newman *et* al., Preceding of Balkan School on Nuclear Physics,
September 1 – 10, 1998 Baltalimani, Istanbul – Turkey, Balkan Physics
Letters, 182 (1998).

[Nil95] Sven Gösta Nilsson and Ingemar Ragnarsson, Shapes and Shells in Nuclear
Structure, Cambridge University; Department of Mathematical Physics,
Lund Institute of Technology, First published 1995. Page 206

[Pau95] E. S. Paul et al., TASCC – P – 95 – 13, Phys. Rev. C

[Rin80] Peter Ring / Schuck, The Nuclear Many – Body Problems, © 1980 by

Springer – Verlag New York Inc, Printed in the United Stetes of America, Page 126 and 127.

[Rad95] D.C Radford, Nucl. Instrum, Methods Phys. Res. A 361, 297 (1995)

[Reg00] Course Notes Post Graduate Nuclear Experimental Techniques (4NET) by Dr P Regan, University of Surrey. (October 2000) Pages 10, 11 and 20.

[Rev92] W. Reviol *et* al., Nucl. Phys. A548 (1992) 331 – 351.

[Rou01] David Gerhardus Roux, PhD thesis, University of Cape Town (April 2001)

[Szy83] Z. Szymanski, Fast Nuclear Rotational, Clarendon press, Oxford, (1983)

[Tim03] J. Timar et al., Eur. Phys. J. A 16, 1 – 5 (2003).

[Voi83] M.J de Voigt *et* al., Rev. Mod. Phys. 55, 949 (1983)

[Vym03] P. A. Vymers, M.Sc thesis, Department of Physics, University of the Western Cape.

[Wil82] J. Wilczynski *et*. *al*., Nucl. Phys. A 373 (1982) 109

[Wys90] R. Wyss *et al*., Nucl. Phys. A 511, 324 (1990).

[Xie05] C. Y. Xie *et* al., Phys. Rev. C 72, 044302 – 1